TERNARY OXIDE STRUCTURES FOR HIGH TEMPERATURE LUBRICATION

Jingjing Gu, B.E.

Thesis Prepared for the Degree of

MASTER OF SCIENCE

UNIVERSITY OF NORTH TEXAS

August 2015

APPROVED:

Samir Aouadi, Major Professor
Peter Collins, Committee Member
Jincheng Du, Committtee Member
Marcus Young, Committee Member
Andrey Voevodin, Chair of the Department of
        Materials Science and Engineering
Costas Tsatsoulis, Interim Dean of the Toulouse
        Graduate School

Gu, Jingjing. *Ternary Oxide Structures for High Temperature Lubrication.* Master of Science (Materials Science and Engineering), August 2015, 64 pp., 7 tables, 30 figures, 67 numbered references.

In this research, a temperature dependent tribological investigation of selected ternary oxides was undertaken. Based on the promising results of previous studies on silver based ternary oxides, copper based ternary oxides were selected to conduct a comparative study since both copper and silver are located in the same group in the periodic table of the elements. Two methods were used to create ternary oxides: (i) solid chemical synthesis to create powders and (ii) sputtering to produce thin films.

X-ray diffraction was used to explore the evolution of phases, chemical properties, and structural properties of the coatings before and after tribotesting. Scanning electron microscopy, Auger scanning nanoprobe spectroscopy, and X-ray photoelectron spectroscopy were used to investigate the chemical and morphological properties of these materials after sliding tests. These techniques revealed that chameleon coatings of copper ternary oxides produce a friction coefficient of 0.23 when wear tested at 430 °C. The low friction is due to the formation of copper tantalate phase and copper in the coatings. All sputtering coatings showed similar tribological properties up to 430 °C.

ACKNOWLEDGEMENT

There are no proper words to express my gratitude to Dr. Samir Aouadi for providing me all of the support, advice, and opportunities though these two years of research. Thanks to him for encouraging me to have my own opinion about this research. I would also like acknowledge my colleague D'arcy Stone for training and helping me in many aspects of this research.

Thanks to my friends for helping me when I am in trouble.

Last but not least, I really appreciate what my parents did for me. Without their support and encouragement, I cannot go abroad and continue my studies.

TABLE OF CONTENTS

LIST OF TABLES

LIST OF FIGURES

CHAPTER 1

INTRODUCTION

A lubricant is a type of medium which can reduce friction between moving surfaces to mitigate the moving parts' wear. The role of the lubricant is to protect a major component. An ideal lubricant has a high boiling point and a low freezing point. The characteristics of a lubricant are thermal stability and corrosion prevention. [1]

The typical lubricants can be categorized to four main types which are water, oil, grease, and solid lubricants. Water and oil lubricants are included in liquid lubricants, and grease and solid lubricants are contained in non-liquid lubricants. [2] Compared to liquid and grease lubricants which have sealing problems or other limitations, solid lubricants can be used in very severe service conditions, such as extreme high or low temperature, vacuum, radiation, ultra contact pressure, high loads, high speed, aerospace, and so on. [3] Although the history of solid lubricant is not long, its excellent performance for lubrication has been widely approved. Therefore, the application of solid lubricants is widespread (automobile, optical equipment, food-processing machines, and so on) [4], and is especially important in the aircraft, aerospace and nuclear power industries. [5]

Aircraft, satellites, spacecraft, and other aerospace crafts work under radiation, vacuum, high speed, extreme temperature fluctuations, or space environment during their service period [4]. Most friction pairs of the transmission components in the mechanical systems (bearings, fasteners, tracking antennas, turbomachinery, gas turbines, hot adiabatic diesel engines, etc.) operate in special conditions; therefore, the friction situation is also unique [6,7]. The low friction

behavior of a solid lubricant in one environment may not appear in another. For instance, graphite can exhibit low friction in humid air but not in vacuum. When designing these friction pairs for mechanical systems, different working conditions and tribological characteristics need to be considered. Finally, a solid lubricant having good friction and wear performance under changing environment is desirable. [8]

Selecting proper material, designing manufacturing method, and creating desired coating to satisfy the requirements of the above fields is a complex problem. For industrial applications, the characteristics of the solid lubricant will depend on the different varying environment, because the variety of surrounding environment (ambient temperature, pressure, etc.) can influence the coefficient friction and lifetime of the solid lubricant [9]. For this research, different materials and methods were selected to produce ternary oxide solid lubricants, and they are tested under diverse operating conditions in terms of temperature. As such, the design of these ternary oxide solid lubricants needs to be optimized to obtain the desired tribology and mechanical performance in a changing environment. The focus of this research is to evaluate their wear performance and friction properties by experimental investigation in varying environment, thus improve the design and production of these solid lubricants.

1.1   Tribology

Tribology is the study and application of the relative friction motion, lubrication, and wear between the surfaces in contact. It is an edge discipline between physics, chemistry, mechanical engineering, and material science. [3] Reviewing the history of tribological

development, tribology has gone through several different historical periods and research modes. Early tribological research was represented by Amontons and Coulomb's studies about solid lubrication. They summarized classic formulas of sliding friction by a large number of experiments. Up to the end of nineteenth century, Osborne Reynolds established the Reynolds' equation which theoretically interpreted the mechanical properties of fluid lubrication film according to the viscous flow mechanism of the lubrication film in the sliding bearing system. [10,11] Since then, the basic hydrodynamic lubrication theory was developed, thus a new research model based on continuum mechanics was created [10]. From the beginning of the 20th century to the present day, due to the demand for production development, research in the field of tribology has tremendously expanded [12]. In 1964, Bowden and Tabor proposed another tribological mechanism based on interface adhesion effect. According to the existence of asperities, they also established a model that shearing occurs in translational motion and adhesion occurs in asperity contacts. [3]

Both physical and chemical phenomena dominating the friction in moving contacts occur at the surfaces of the solids during relative movement. Typically, the interaction mechanisms of the outermost layers are the most important for the tribological properties. One way (the most common way for a long time) to change the tribological performance of two relative moving surfaces is to add a fluid between the surfaces. Another way is to introduce a thin layer or surface coating on one side or both sides of the relative moving surfaces. This kind of thin films can be fabricated by physical vapor deposition (PVD) and chemical vapor deposition (CVD) techniques.

For metallic and ceramic coatings, the tribological process not only changes the geometry

and composition of the material with time, but also leads to the occurrence of friction, wear,

velocity, temperature, sound, and dynamic behavior. The complete tribological process in

moving contacts in relative motion is very complicated because different types of friction, wear,

and deformation will simultaneously occur at different scale levels. In order to holistically

analyze the complete tribological process and understand the interactions, the tribological

transformations are divided to four different types which are the macromechanical effects, the

micromechanical effects, the chemical effects, and the material transfer (Fig. 1). [3]
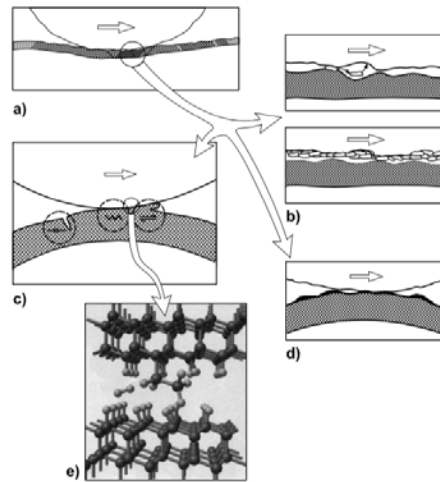
FIG 1 Tribological contact mechanisms: (a) macromechanical, (b) material transfer, (c) micromechanical, (d) tribochemical, and (e) nanophysical. [3]

The macromechanical tribological mechanisms of coated surfaces demonstrate the

friction and wear phenomena. The influence factors of these mechanisms are the distribution of

the stress and strain for the entire contact, the resulted total elastic and plastic deformations, and

the forming process and dynamics of the wear particles. The hardness relationship of

coating-to-substrate, coating thickness, surface roughness, and the debris' size and hardness are

the four primary parameters that determine and control the tribological contact behavior between

the one or both coated contact surfaces. Different contact conditions based on particular

tribological mechanisms depend on the relationship of these parameters (Fig. 2). [3]
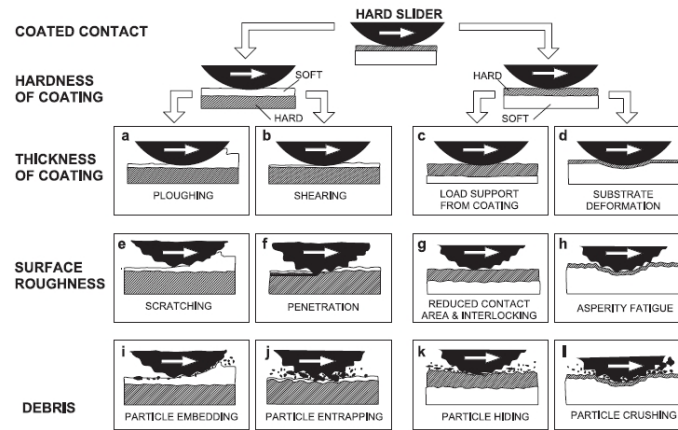
FIG 2 Macromechanical contact conditions for different mechanisms that influence friction when a hard spherical slider moves on a coated flat surface. [3]

When the friction and wear phenomena occure at a size level $\leq 1\mu m$ (down to nanoscale),

the micromechanical tribological mechanisms will be applied to describe the stress and strain

formation at a asperity level, the generation and propagation of cracks, material liberation, and

single particle formation (Fig. 1 (c)). The nanoscale tribology studies the mechanisms and

phenomena of the two relative moving contacting solids ranging from microscale to nanoscale [10].

Krim proposed that friction is generated from atomic lattice vibration while the surface atoms

participate in the opposite sliding motion. Tervo claimed that the surface lattice vibration will

increase friction during sliding. [3]

Tribochemistry involves chemical reactions that occur at sliding surfaces during the

tribological process. During the tribochemical reactions, the composition of the interface and its

mechanical properties vary monotonously. During the mechanical process (mainly milling

progress), the local temperature at the relative sliding surface can be over 1000□C due to the

mechanical energy, and this temperature will provide the thermal energy to create chemical

reactions at the interface between the two sliding surfaces. For example, because of the thermal

energy, the bonds in the outermost surface material will break, then some hard phase will

transfer to the amorphous phase (low-shear microfilms). Moreover, the pressure at the contact

area is also higher than the surroundings. [3,13] For very high temperature (>500□C), the hard

phase with metal additions can be oxidized to form stable oxide layers which have low friction

coefficients (0.3-0.6). This reaction is called tribo-oxidation. [14] The thickness of these oxide

layers is about 1-10nm. Some of the oxide layers, such as copper oxide, are more prone to shear,

while the others, such as aluminium oxide, show the opposite characteristic (i.e. harder). [15] This

tribo-oxidation mechanism is applied as the basis of this research.

For the material transfer, if particles were released from the surface, they can form debris,

and they can affect the tribological properties of the contacting surfaces in two different

mechanisms; (i) the loose debris will influence the friction and wear of the contacting surface;

and (ii) the debris adheres to the counterface to form a new active surface having new

tribological properties. [15]

1.2   Solid Lubricants

Solid lubricants are substances that exist between sliding solid surface that do not involve

a liquid medium. One classification divided solid lubricants into intrinsic and extrinsic solid

lubricants [16]. The intrinsic lubricants have an easily sheared atomic structure, thus interfacial

6

sliding motion can be promoted. The extrinsic ones are influenced by the active additives from

the surroundings to obtain the low shear properties. [16] Common solid lubricants are graphite,

molybdenum disulfide, the transition metals, and so on, which have a lamellar or layered

structure. In fact, most of the solid lubricants possess the lamellar structure. The others (e.g., soft

metals, polytetrafluroethylene, polyimide, certain oxides and rare-earth fluorides, diamond and

diamond-like carbons [DLC], fullerenes) are non-lamellar crystal structure. [3]

However, traditional solid lubricants have some shortcomings at high temperature. The

first one is that most solid lubricants have low thermal conductivity which will generate heat

locally except of soft metals. Secondly, the friction coefficients, and wear ratio are high

compared to other lubricants, which will not provide protection to the sliding surfaces. Finally,

they may undergo irreversible structural or chemistry changes which can lead to loss of lubricity,

and poor adhesion. For instance, MoS_2 coatings are soft, and have poor adhesion. Soft metals

have poor wear properties. DLC coatings are brittle due to the high internal stresses, and have

poor adhesion. As a result, it is necessary to invent a true solid lubricant with both low friction

and wear resistance to obtain the optimum wear protection. The final result is that the effect of

the solid lubricants is the same way as the liquid counterparts at the relative motion surface. For

this reason, a new kind of solid lubricant which is called oxide solid lubricant was invented. [17,18]

Oxide solid lubricants which are also called lubricious oxides were shown to be lubricious at

elevated temperatures. [19]

Oxide solid lubricants are oxides which certain metals or metalloids (e.g., Re, Ti, Mo, Zn,

V, W, B, etc.). Moreover, some mixed oxides (e.g., $CuO-Re_2O_7$, $CuOMoO_3$, $PbO-B_2O_3$,

PbO-MoO$_3$, CoO-MoO$_3$, Cs$_2$O-MoO$_3$, NiO-MoO$_3$) which can be produced as alloys or composite structures also have low friction coefficient and long durability. Oxide-based self-lubricating materials can be fabricated by appropriate coatings (by means of PVD, plasma spraying, fusion bonding, etc.). They can be also mixed with other solid lubricants, so they can be used in wider temperature ranges. [3,20]

At ambient temperature, the lubricious oxides are brittle and unable to plastically deform because of the repulsive motion of the charged ions and the large distance of Burger vector. However, at elevated temperature, oxides have been plastically deformed to mitigate the friction. Along with the oxide layers that are depleted by wear, the alloying ingredients will diffuse to the higher oxygen potential surface; then the oxidization will reoccur to replenish the consumed lubricious layers. Therefore, most oxide-based lubricants cannot meet the solid lubricant requirement at room temperature. A suitable application area for oxide-based solid lubricants is high-temperature seals, bearings, gears, valves, and variable stator vanes. [20-22]

Ternary oxide lubricants can generate Magnéli phases during tribology process at high temperature. Magnéli phases are the homologous series of Me_nO_{2n-1}, Me_nO_{3n-1}, or Me_nO_{3n-2} compounds formed by some transition metals' substoichiometric oxides. In Magnéli phases, crystallographic shear planes will be formed by planar lattice faults to reduce the binding strength. [14] Gardos discovered that the generation of Magnéli phases on the surfaces of the oxides, forming anion-deficient phases, can improve the friction and wear properties of these surfaces. [23] The transition metals and the noble metals are always combined to create the ternary oxide lubricants for high temperature application [16].

Table 1 Oxide Solid Lubricant with Self-lubricating Capability [3]

Classification	Key Examples	Typical Range of Friction Coefficient
Single-Oxides	B_2O_3	0.15–0.6
	Re_2O_7	0.2
	MoO_3	0.2
	TiO_2 (sub-stoichiometric)	0.1
	ZnO	0.1–0.6
Mixed Oxides	$CuO–Re_2O_7$	0.3–0.1
	$CuO–MoO_3$	0.35–0.2
	$PbO–B_2O_3$	0.2–0.1
	$CoO–MoO_3$	0.47–0.2
	$Cs_2O–MoO_3$	0.18
	$NiO–MoO_3$	0.3–0.2
	$Cs_2O–SiO_2$	0.1

1.3   Nanocomposite Coatings

The coatings of nano-crystallites embedded in an amorphous matrix are named

nanocomposite coatings [24]. According to the Hall-Petch relation, decreasing grain size can

reinforce the hardness, fatigue resistence, and the yield strength of the amorphous material due to

grain boundary hardening [3,25]. A nanocomposite coating is composed by two phases (a

nanocrystalline phase combined with an amorphous phase, or two nanocrystalline phases) at

least (Fig. 3). Different nanocomposite coatings will show different hardness properties from

hard to ultra-hard (20 GPa-80 GPa). [26]
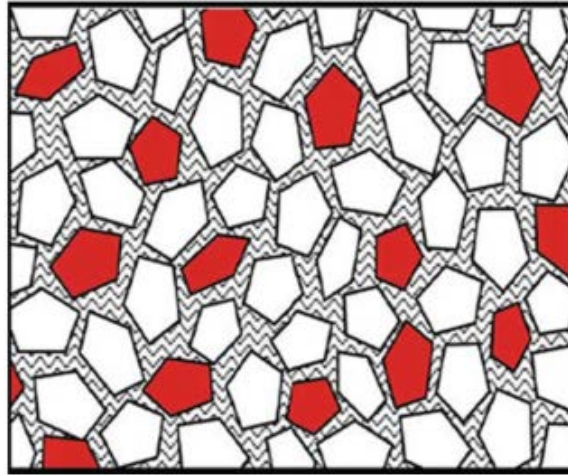
FIG 3 Microstructure of nanocomposite coating. Nanocrystalline phase: hexagons; Amorphous
phase: waves. [14]

For bulk materials, according to the Hall-Petch relation, the hardness of the material is

increased with grain size decrease, because the mobility of the dislocations is impeded. However,

if the grain size of the crystallites is less than 10 nm, the strength of the material will decrease

when the grain size decreases due to the sliding motion of grain boundary. Therefore, this

softening phenomenon will result in the formation of large amounts of defects in grain

boundaries, thus atoms and vacancies can diffuse fast. (Fig. 4) [26]
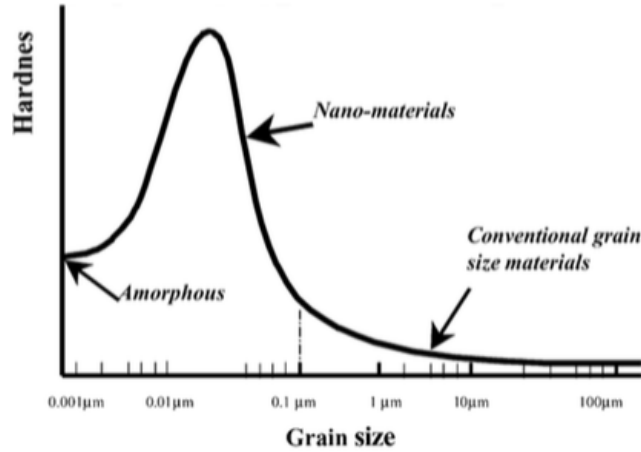
FIG 4 Hardness of a material as a function of the grain size. [26]

In order to improve hardness of the material, grain boundary sliding should be impeded. The toughness of the material is also required, so it is necessary to retain a certain degree of grain boundary diffusion and sliding. One method is combining more nanocrystalline phases to create complex boundaries, but the toughness cannot be efficiently improved because of the impedence of dislocation movement. Another one is embedding nanocrystallites in an amorphous matrix. For this method, the nanocrystalline grains should be oriented randomly, and the amorphous matrix should have flexible structure. The third method is by creating more complex systems (i.e. ternary, quaternary, or even more complicated systems). They contain a high strength amorphous matrix and hard transition metallic compound (i.e. ceramic) nanocrystallites as crystalline phase. [26]

1.4   Chameleon Coatings

Chameleon coatings, also called adaptive coatings combine multiple solid lubricant to

make nanocomposite coatings [14]. These coatings can provide good tribological properties by change their structure and/or chemistry to satisfy the requirement of multiple environments [8]. They can be applied in a broad-range of temperatures as well as in air to space environments [14].

According to the nanocomposite coating concept, selecting coating composition to enable self-release for every anticipated environment and providing a method to guide nanoscopic volume in the contacting area satisfy macroscopic solid lubricate's formation [14]. The adaptive mechanisms can be categorized to three types: metal lubricants diffuse to the surface, lubricious oxide phases form (tribo-oxidation), and structure of the lubricant changes (structural transtion). [27]

CHAPTER 2

OBJECTIVE AND METHODOLOGY

The purpose of this research is to create ternary oxide coatings that have adaptive

properties to maintain superior performance at high temperatures (beyond 350 °C), and that

perform well at low temperatures (25 °C – 350 °C). Recently, many successful ternary oxides

combining transition metals and soft metals ($SM_xTM_yO_z$: SM represents soft metal, TM

represents transitional metal) to create lubricants for high temperature applications exhibited low

friction coefficients (about 0.1-0.4) from low temperature to high temperature [16,27,28]. Ag, Cu, Au,

In, Pb, and Zn were always selected as soft metal dopants [29]. Our group has recently investigated

the tribology properties of lubricious perovskite silver tantalate ($AgTaO_3$) throughout the

temperature range that varies from 25 °C to 750 °C. The perovskite silver tantalate has a layered

structure, and its melting temperature is 1172 °C, which is relatively high. During the

temperature-rise period, the structure of silver tantalate changes, and its surface structure

reconstructured. [29] At 750 °C, the friction coefficient of $AgTaO_3$ can reach 0.06 due to the

formation of nanocrystalline Ag, Ta_2O_5, and $AgTaO_3$ phases mixed layer at the sliding surfaces

[30]. The nanoparticles of silver also present and aggregate to form clusters and they maybe

advantage to increase coating toughness [29]. However, the high diffusion rate of silver at high

temperatures results in the potential for silver contaminate surrounding components. [31,32] Based

on these promising results, copper has been selected as a substitute for silver to obtain both good

friction and wear performance. This investigation focused on copper based ternary oxides to

understand the tribological behavior of these solid lubricants at a relatively wide temperature range.

2.1 Copper Based Ternary Oxides

Cu-Ta-O was selected for the following reasons: (1) both copper and silver are located in the same group IB (11) of the periodic table of the elements, which are commonly called the copper subgroup [33]; (2) both copper and silver have face-centered cubic crystal structures, which means that they have 12 slip systems [34]; (3) both copper and silver are soft metals, and they have good ductility [3]; (4) $CuTaO_3$ and $AgTaO_3$ compounds have the same perovskite crystal structure which possesses numerous interesting and helpful properties [29,35]; (5) the friction coefficients of copper and silver are close under varying environments (Table. 2) [3]; (6) the melting point of copper is higher than that of silver (the melting point of copper is 1084.62 °C, and the melting point of silver is 961.78 °C) [33]; (7) both copper and silver have good thermal conductivity; (8) both copper-based oxides and silver-based oxides have been investigated as potential solid lubricants [37]; (9) they were both produced from soft metals and the nanocomposites of transitional metal oxides [29]; and (10) copper is less expensive than silver which will reduce the cost of its industrial manufacturing.

For this reasearch, we focused on the two kinds of copper-based ternary oxides which are $CuTaO_3$ and $CuTa_2O_6$. Not only experimental studies but also theoretical studies were investigated to understand and optimize the structural and mechanical properties of the oxide lubricants. For the experimental method, $CuTa_2O_6$ was produced to study the influence of copper dopants on the

frictional and wear properties of Cu-Ta-O solid lubricants. For the theoretical method, Hongyu

Gao and Ashlie Martini, in collaboration with our group, used molecular dynamics simulation (see

appendix A) to identify the effect of copper dopants and the results of the tribological performance

of Cu-Ta-O lubricant by selecting $CuTaO_3$ and $CuTa_2O_6$. According to the recently research that

$AgTaO_3$ has better tribological performance than $Ag_2Ta_4O_{11}$ [29], the friction properties of Cu-Ta-O

oxides and Ag-Ta-O oxides are also compared to obtain high performance solid lubricant from low

temperature to high temperature.

Table 2 Friction of Metals (Spectroscopically Pure) Outgassed in Vacuum. [36]

Metals	Coefficient of Friction after Admitting		
	H_2 or N_2	Air or O_2	Water Vapor
Aluminum on aluminum	—	1.9	1.1
Copper on copper	4	1.6	1.6
Gold on gold	4	2.8	2.5
Iron on iron	—	1.2	1.2
Molybdenum on molybdenum	—	0.8	0.8
Nickel on nickel	5	3	1.6
Platinum on platinum	—	3	3
Silver on silver	—	1.5	1.5

2.2 Adaptive Coatings (Chameleon Coatings)

Coatings of Cu/Ta_2O_5, Cu/Ta were created as potential nanocomposite chameleon

coatings. Because the tribological performance of Cu-Ta-O oxides has not been studied yet, we

assumed that copper clusters in the outermost surface might promote the relative sliding between

the two contacting interfaces due to the lubrication mechanisms of Ag-Ta-O oxides (silver

diffused to the surface and provided lubrication) between 350 °C to 500 °C (i.e. moderate

15

temperature). For high temperature applications, copper, copper oxides, and binary metal oxide phases may form at the sliding surfaces and provide the required lubrication. [29]

The melting point of $AgTaO_3$ is 1172 °C, but the melting point of $CuTaO_3$ is unknown because they were not explored except for their electrical properties. [38,39] In this research, different parameters were selected to produce burnished powder coatings of Cu/Ta_2O_5 and sputtering coatings. After that, they were examined by X-ray diffraction (XRD) before and after wear testing to analyze the chemical and structural transformation of the coating surface.

CHAPTER 3

EXPERIMENTAL TECHNIQUES

The investigation of the tribological performance of copper based solid lubricants

consists of to the creation of the required coatings and their characterization. Many different

methods including chemical vapor deposition, physical vapor deposition, electroplating,

chemical plating, and external painting used to create the tribological thin solid films. [3,41] In this

study, two methods were used to create copper tantalate thin films. One is the magnetron

sputtering technique, which is the most appropriate technique to synthesize these thin films.

Another method is burnishing copper tantalate powder on a flat substrate prior to tribotesting.

The method of producing copper tantalate powders is termed the solid state synthesis

technique[29].

The tribological behavior and performance of the coatings depend on the characterization

of the crystal structure, chemical properties, surface structure and topography, frictional

properties as a function of surrounding environment and ambient temperature. As a result, X-ray

diffraction is used to analyze crystal structure, elements, and phase composition. Scanning

electron microscopy is used to analyze surface morphology. An Auger scanning nanoprobe is

used to analyze elemental and chemical composition. X-ray photoelectron spectroscopy is used

to inspect molecular composition and chemical bonding. Pin-on-disk tribometer test is used to

evaluate the frictional performance of the thin films.

3.1 Unbalanced Magnetron Sputtering

Sputter deposition (sputtering) is a widely used technique to deposit a thin film on the

surface of the substrate by creating high energy particles in a vacuum chamber. According to

energy transfer, the high energy particles made by the high voltage applied non-reactive gas

bombard the surface of the target material, then the atoms or molecules at the surface of the

target material escape and are accelerated to be deposited on the surface of the substrate (Fig. 5).

[40-43]
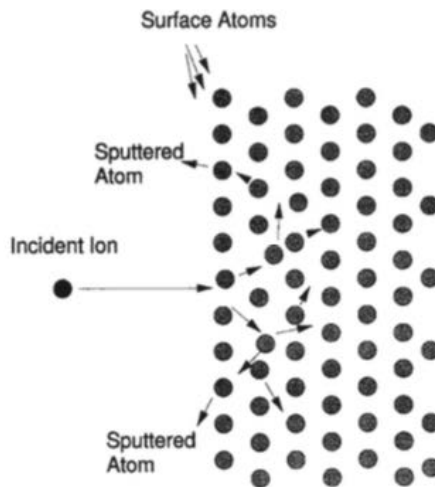
FIG 5 Schematic of physical sputtering process. [43]

Sputtering can be categorized to two types. One is called ion beam sputtering whereby an

ion beam bombards the surface of a target to deposit sputtered particles on the substrate. This

technology is relatively expensive, and it is mainly used to produce some special films. Another

one is called cathode sputtering which uses a plasma to bombard the target to obtain the

sputtered particles. [40-42] Either inert gas ions (argon or krypton) or small molecular gas (nitrogen

18

or oxygen) are involved in the ion bombardment [43]. Sputtering techniques can be classified to cold cathode DC diode sputtering, DC triode sputtering, AC sputtering, RF sputtering, DC magnetron sputtering, pulsed DC magnetron sputtering, and ion and plasma beam sputtering [40]. For this research, magnetron sputtering was used to produce ternary oxide lubricious films because it can create good adhesive and flat films and allow non-thermally evaporated material to be used [40].

In a sputtering system, the target plate is the cathode, and the substrate will be the anode. During the sputtering process, the argon ions bombarding the target surface will also generate secondary electrons at the same time to maintain the plasma. For magnetron sputtering systems, the arrangement of the magnets is that one pole is placed at the center of the target, and the second pole is a ring of magnets located around the outside edge of the target. The function of these magnets is to constrain secondary electron motion near the target by forming a magnetic field parallel to the surface of the target. This method will promote the collision between electrons and target surface atoms, and maintain dense plasma to increase ion bombardment. Consequently, the sputtering rate and deposition rate will be increased. [44]

For balanced magnetic field, the magnetic field lines are closed at the target surface to constrain the electrons near the target surface, so the low ion bombardment results in low density plasmas near the substrate. As a result, unbalanced magnetrons in which magnetic field lines are not completely closed at the target surface by strengthening or weakening one magnet compared to the other one was invented to enhance the plasmas density near the substrate and thus change the structure and properties of the deposited films (i.e. dense films), as seen in Fig. 6. [44,45]

Unbalanced magnetron sputtering is commonly applied to deposit hard and wear-resistant

coatings [42]. The relationship between approximate sputter yields for experimental material and

iron energies of argon iron bombardment is given in the following table (Table 3) [43].
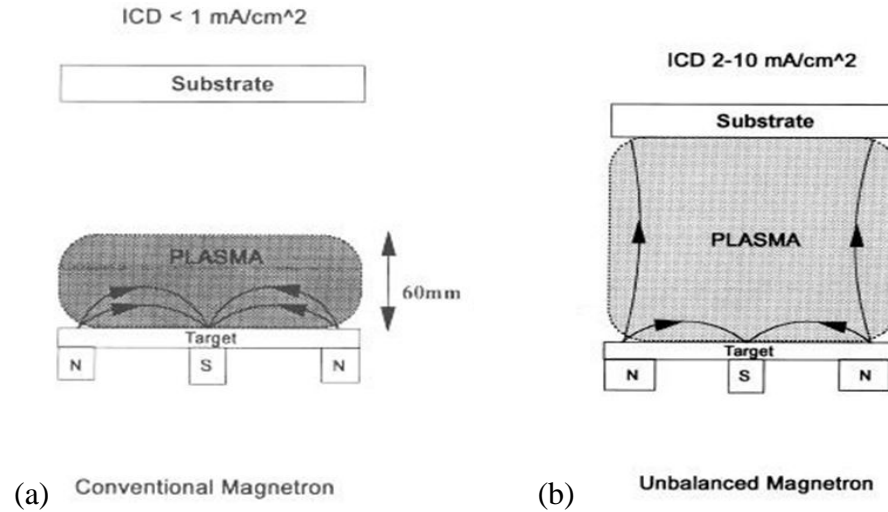
FIG 6 Schematic representation of the two types of the magnetron sputtering. (a) Conventional
magnetron (balanced). (b) Unbalanced magnetron (unbalanced). [45]

Table 3 Sputter Yields as A Function of Ar Ion Energy for Commonly Used Materials

Material	300eV	500eV	1000ev
Ag	1.7	2.5	3.5
Cu	1.5	1.9	2.9
Ta	0.3	0.5	0.9

If oxygen or nitrogen is introduced into the vacuum chamber of the sputter machine, they

will react with the sputtered material when they move towards the substrate to create a

compound coating. This phenomenon is called reactive sputter deposition. Another kind of

reactive sputtering is the use of a co-sputtered target to obtain a compound coating. [40]

3.1.1 Unbalanced Magnetron Sputtering Equipment

Before the sputtering process, the chamber is pumped down to 10^{-4}-10^{-8} Pa (base pressure)

to reduce contamination of the coating. A high purity argon flow controlled by a flow meter is

continuously injected into the vacuum chamber to obtain the equilibrium pressure between 5 to 7

Pa and then the glow discharge is struck to promote the iron bombardment. A negative RF or DC

voltage is applied to the target starting the sputtering process. An RF bias is applied to the

substrate. The substrate is rotated to gain a uniform coating on the substrate surface. (As shown

in Fig. 7(a))

(a)   (b)
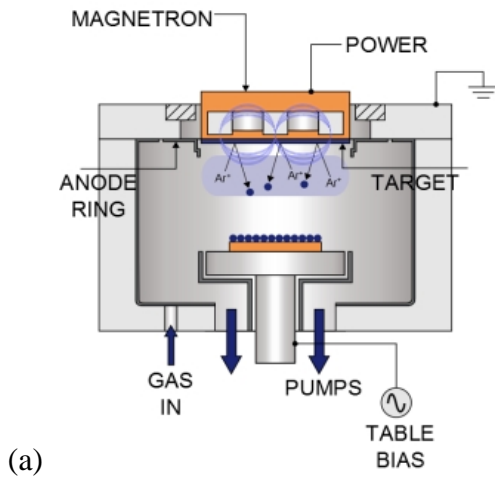
FIG 7 (a) A schematic representation of the magnetron sputtering system [46]; (b) AJA A300 series
magnetron sputtering sources.

3.1.2 Unbalanced Magnetron Sputtering Experimental Details

In this research, ATC 1500 magnetron sputtering machine (AJA International, North

Scituate, MA) was used to produce Cu-Ta-O ternary oxide coatings on mechanically polished Inconel 718 substrates.

Firstly, all of the substrates were ultrasonically cleaned in acetone and methanol respectively for 10 minutes each wash. After clean step, they were rinsed in deionized water and dried by compressed nitrogen before put them into the vacuum chamber. Then the magnetron sputtering system was pumped down to a base pressure below 10^{-5} Pa after insertion of the substrate into the chamber. When the base pressure is reached, the substrates were heated to 550 °C, then Ar (99.999% purity) was imported into the vacuum chamber. The gas valve is manually rotated to obtain a partial pressure of 5 Pa. Subsequently, a bias of -260 V was used to etch the substrates for 15 minutes to remove the contaminats on the surface of the substrates which could affect coating adhesion. After etching, the bias to the substrate was decreased to -70 V for film deposition. The deposition process was completed in 1.5 hours. [29]

Elemental targets of Ta (99.95% purity) and Cu (99.999% purity) were used as the starting materials. The experimental method of co-sputtering was achieved by using Cu and Ta targets in a mixed atmosphere of Ar and O_2 (reactive gas) to create compound coatings. Other sputtering parameters are shown in Table 4.

Table 4 Sputtering Parameters for Cu-Ta-O Ternary Oxides

Sample	P_{Cu} (W)	P_{Ta} (W)	P_{O2} (mTorr)
S1	80	58	2.0
S2	70	58	2.0
S3	90	58	2.0

3.2   Solid State Sythnesis

Mixing, pressing, and heating powders to promote their reaction with each other is a

simple and widely used method to produce inorganic solids. This method was named solid state

reaction. The formation reaction takes a long time to finish because of the slow diffusion of the

ions such as Mg^{2+} and Al^{3+}. Therefore, high temperature heat treatment is required to help ions

diffusion by providing sufficient thermal energy. The diffusion mode of the ions is through

hopping out of one site and inserting into an adjacent vacancy or interstitial site. [47]

Grinding is one significant way to accelerate the reactions of the powder mixtures to

break the surface of the particles. Breaking the interfaces between reactants and products can

bring new reactant surfaces into contact, thus helping mixtures' reactions. Another efficient

solution to improve solid reactions is introducing gas- or liquid-phase to assist transportation of

compositions, and bring reactants together. This method does not require a long time for solid

state diffusion. Therefore, adding a little liquid transporting agent to the powder mixtures during

the grinding process may improve the efficiency of the solid state reactions. [47]

If one or more reactants are chemically active, or their containing ions diffuse easily,

solid state reactions could happen easily. In order to plan a solid reaction, selecting reactive

material, choosing mixing method, picking proper container, and designing heat treatment are the

four key issues to consider. [47]

3.2.1   Starting Materials

Under the premise of knowing the stoichiometry accurately, the pure and reactive

material should be known ahead of time. Few of the reactants may need to be dried firstly. For oxide synthesis, carbonates, acetates, or nitrates, which belong to the oxy salt reactants (except sulfates because of their thermal stable), can be helpful because they can decompose during heating. The decomposition process can increase surface area of the particles by decreasing their size to improve reactivity. [47]

3.2.2 Mixing Method

Mixing and milling can improve the contacting surface area of the reactants. Manually grinding by using mortar and pestle and mechanical grinding such as ball milling are be applied. For manual grinding, agate mortar and pestle are ideal because of their non-porous and not contaminate samples properties. For mechanical grinding, the reactants and some agate balls are put into a rotating container together. Both manual method and mechanical method need to add liquid agents such as water or an organic liquid, and they will be evaporated in a subsequent drying process. [47]

3.2.3 Container

The containers should not react with the samples. Crucible or boats of Pt, Au, Al_2O_3, SiO_2, and graphite are commonly used containers. Gaphite crucibles are usually applied to sulfides, nitrides, and other chalcogenides. [47]

3.2.4 Heat Treatment

The heat treatment design should obey the following principles. Firstly, oxy salt reagents mildly decompose instead of excessive frothing, melting, or leakage from the container. Melting and volatilization of the reactants must be avoided. Lastly, reactants react during a reasonable timescale (e.g.12-24 hours) under applied temperature. [47]

According to the above principles, many inorganic solids can be perfectly created by solid state reaction. [47]

3.2.5 Solid State Sythnesis Experimental Details

Copper tantalate powders were synthesis by solid state reaction method. In this research, tantalum oxide (99.993% purity) and copper (99 % purity) powder were dried in a furnace at 150 °C for 2 hours. The quality of the powders obeys the principles of stoichiometric ratios. Grinding was applied by agate mortar and pestle to obtain homogenous samples in isopropanol of 70% concentration for 4.5 hours. The grinding finished powder in a quartz crucible was calcinated at 850 °C and 1000 °C for 16 hours to produce Cu-Ta-O ternary oxide. After calcination, the powder samples were burnished on Inconel 718 substrates. The aim of burnishing the powders is to make a flat coating on the surface of the substrate. [29,48]

However, after 1 hour, the powders did not adhere to the substrate surface without burnishing the surface of the substrate. As a result, the powders were knocked on the surface by pestle to make an evenly coating. Other parameters of solid state synthesis are shown in Table 5.

Table 5 Parameters of Solid State Synthesis for Cu-Ta-O Ternary Oxides

Sample	Cu (g)	Ta$_2$O$_5$ (g)	Temperature (°C)
G1	1.28	4.42	850
G2	0.854	4.027	850
G3	1.28	2.21	1000

3.3 Wear Testing

Measuring the force (F) initiating and sustaining sliding and the normal force (N) maintaining the contacting of two surfaces provides the value for the coefficient of friction. [3] The initiating and sustaining force (F) and the normal force (N) can be obtained by applying a load normal to the surface to the test samples.

For the pin-on-disc tribometer, a cantilever-shaped force transducer (i.e. an arm including an internal load sensor) holds a round-tip pin. The pin slides against the disk. A driven system is applied to rotate the disk. A pedestal sits under the disk to hold the disk. [3] When the disk rotates, the arm will have a slight deflection. The deflection will create a signal propagating to the sensor inside the arm. The deflection will be received by the sensor, then translated to voltage and recorded.
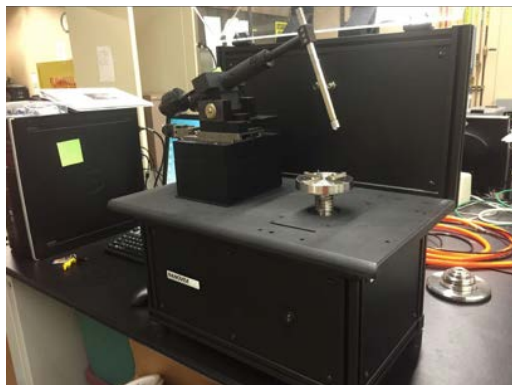
FIG 8 Nanovea pin-on-disk tribometer.

3.3.1 Wear Testing Experimental Details

In this experiment, a Nanovea Tribometer was used to test the coefficients of friction from room temperature to 430 °C by using a silicon nitride (Si_3N_4) ball at 200 RPM. A 2N load was applied for all wear tests. A large removable oven can heat the rotation test to high temperature. Room temperature, 200 °C, and 430 °C were chosen to test the tribological performance of the samples.

3.4 X-Ray Diffraction

X-ray diffraction (XRD) is a nondestructive technique to identify the various kinds of crystalline phases in solid materials and powders. The crystal structure and particle size of the material can also be determined. In scientific research, this technique is widely applied to study nanostructured thin films and nanoparticles. While X-rays are incident the crystalline sample, a part of them will be diffracted to form XRD patterns. These patterns express the particular information of the sample. The international database containing reference patterns will be used

to analyze the XRD patterns of the sample by comparing them. By using the XRD technique, the

intrinsic properties and external performance of the materials are linked. [49] In our research, the

International Center of Diffraction Data (ICDD) database was utilized.
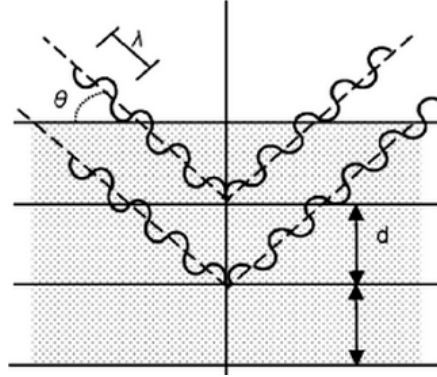
FIG 9 Condition for constructive interference. [49]

In crystallography, the atoms of solids have an order distribution in three-dimensional space.

This phenomenon will result in the formation of a series of parallel planes having interplanar

spacing. The number of the interplanar spacing varies for different materials. While an X-ray

beam with λ wavelength is inciding into a material having spacing d at angle θ, diffraction occurs

if the wavelength of the reflected ray differs from the incident X-ray by an integer number (n) to

generate constructive interference (Fig. 9). This kind of constructive interference can only occur

when they satisfy all conditions of the Bragg's law. By using Bragg's law, the interplanar spacing

can be calculated. The parameter n is an integer, λ is incident wavelength, d is the interplanar

spacing, and θ is Bragg angle. [34,49]

$$n\lambda = 2d\sin\theta \tag{1}$$

The typical XRD patterns are the graphic using the diffracted intensity as the vertical axis

and the detector angle 2θ as the horizontal axis. In ideal conditions, sharp and ordered diffraction

peaks are displayed from the perfect crystals. However, realistic diffraction peaks have a finite

width. The helpful conclusion to predict the particle size is that the width of the peaks is

inversely proportional to the particle size. Therefore, using the width of the diffraction peaks can

determining the crystal size. In XRD experiments, if the crystals are smaller than 1000 Å,

Scherrer equation:

$$t = K\lambda (B\cos\theta)^{-1} \qquad\qquad (2)$$

is applied to calculate the particle size, where λ is the incident wavelength of X-ray, θ is Bragg

angle, K is a constant depending on the grains shape (usually between 0.9-1), t is the grain size,

and B is the full width at half maximum of the broad peak. [49,50]

3.4.1   XRD Experimental Detail

The experimental X-ray is Cu Kα X-ray which has a wavelength of 1.53 Å. A filter was

used between the sample and the detector [50]. The samples of Cu-Ta-O ternary oxides were

scanned from 30 to 80° for 2θ range on Rigaku Ultima III before and after wear test. For the

powder samples, powders pressed on the glass were scanned before wear tests, and burnished

powder coating on the 718 inconel substrate was tested after wear tests.

3.5   Scanning Electron Microscopy

The secondary electron images of the materials obtained by SEM realize the study of

topography and morphology of materials. The interaction between electron and specimen will

generate X-rays, hence composition can be analyzed by monitoring these X-rays. The electron

beam will be generated from a heated lanthanum hexaboride (LaB_6) or tungsten filament by

applying voltage (Fig. 10). [49,52]
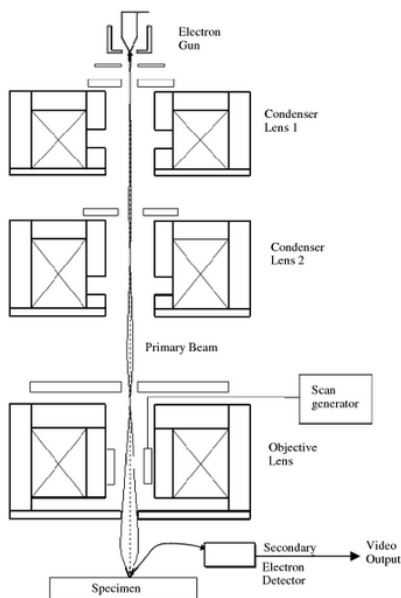
FIG 10 Schematic drawing of a SEM. [52]

3.5.1 SEM Experimental Detail

FEI Quanta 200 ESEM is equipped the Schottky filed emission gun (FEG) [51]. The

sputtering samples of Cu-Ta-O ternary oxides were scanned on Quanta 200 ESEM after wear

tests. The elemental composition of the selected region in the coating was estimated by EDX

after tribotesting.

3.6 Auger Scanning Nanoprobe

Auger scanning nanoprobe is an Auger electron spectroscopy (AES) instrument that

provides elemental and composition information for the outermost surface (2-10 nm) of the

materials [53]. When an electron beam incidents to atoms in the surface of the material, core-level

electron will be excited, and leave a vacancy. Outer-shell electron having high energy will fill

this vacancy, and then another electron (Auger electron) will be ejected by the excess energy. As

shown in Fig. 11, a vacancy in the K-shell is filled by an electron from the L-shell. Excess

angular momentum and energy relax to keep equilibrium state, so an Auger electron is emitted

from the L-shell. [54] Measuring the kinetic energy of Auger electron is used to identify different
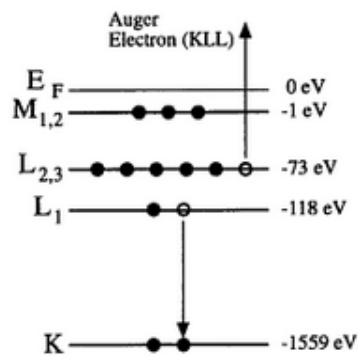
elements. [53]

FIG 11 Illustration of the Auger KLL process for alumium. [54]

Auger electrons can be detected for all elements except helium and hydrogen [40]. The

ionization cross-section of the initial core-level and the Auger relaxation probability determine

the intensity of the Auger transition [54].

3.6.1   Auger Scanning Nanoprobe Experimental Detail

The basic structure of the Auger scanning microprobe instrument is similar to the scanning electron microscope (Fig. 12). An ultra high vacuum system, a detector and energy analyser between 0-2 keV, and a sputter-ion gun are the primary characteristics of Auger systems. [54] PHI 670xi Scanning Nanoprobe was used to analyze the sputtering samples of Cu-Ta-O ternary oxides after wear testing.

Channeltron electron multiplier

Energy resolution aperture
Inner deflection cylinders

Outer deflection cylinder

Sputter ion gun

Coaxial electron gun

Sample

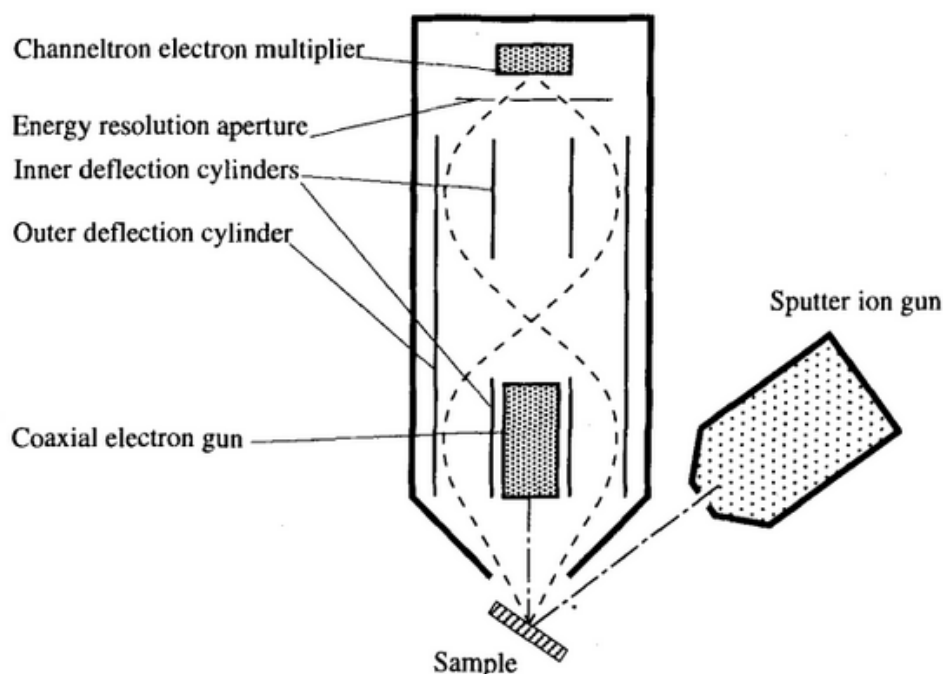FIG 12 Schematic illustration of an Auger system with coaxial arrangement. [54]

3.7   X-ray Photoelectron Spectroscopy

X-ray photoelectron spectroscopy (XPS) reveals the information of the chemical bonding of the composition on the surface of solid materials. The principle of the chemical analyze with electron spectroscopy is that analyze the energy of emitted secondary electrons which excited by

photons, electrons, irons, or neutrals [55]. A core electron bounding to an atom or ion is

ejected by a photon to produce photoelectrons. The energy can be transferred completely during

photon-electron interaction. If the energy is sufficient, the electron emission from the atom or ion

will occur. The kinetic energy of the emitted electron will be measured. [56] Shown in Fig. 13 is a

one electron emission scheme.

The relationship of the binding energy (E_B) and the kinetic energy (E_{kin}) is:

$$E_B = h\upsilon - E_{kin} - \varphi \tag{3}$$

where $h\upsilon$ is the energy of the X-ray (h is Planck's constant, υ is the frequency), and φ is the work

function of the spectrometer. [54]
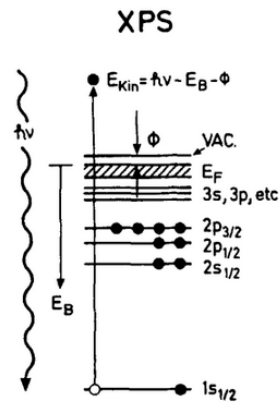
FIG 1 Schematic illusion of photoelectron emission. [54]

1.1.1 XPS Experimental Detail

For this research, PHI 5000 VersaProbe was used. The basic component of XPS apparatus

is similar as AES. The apparatus includes the ultrahigh vacuum chamber with sample stage,

electron energy analyzer and detection system, and the X-ray source, and an iron gun. [55] The

copper, tantalum, and carbon elements were analyzed. Carbon was used as a standard element.

RESULTS

2.1   Crystal Structures

2.1.1   CuTaO$_3$

CuTaO$_3$ has a layered crystal structure, as shown in Fig. 14 [58]. The structure of CuTaO$_3$

belongs to the 3-D trigonal crystal system [34,57]. The space group for it is R3c. The lattice

parameters are a=5.2356 Å and c=13.8631 Å. This structure is similar to LiTaO$_3$. [57] Ta (B)

cations locate at the body center and Cu (A) cations locate at the cube vertices, and O^{2-} anions

occupy the face centers. [34]
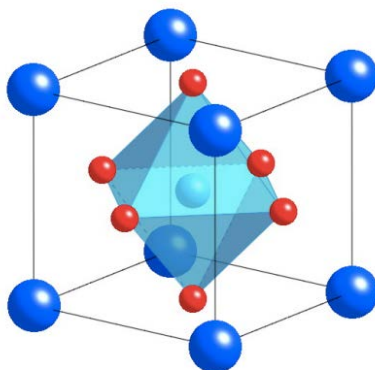
FIG 2 Crystal structure of CuTaO$_3$. [58]

The Cu cations are coordinated with twelve O^{2-} anions to CuO$_{12}$ cuboctahedral, and the

Ta cations are coordinated by six O^{2-} anions to form TaO$_6$ octahedron. [34] The binding energy of

Cu-O is 287.4 ± 11.6 KJ/mol^{-1}. For Ta-O, the binding energy is 782.0 ± 2.5 KJ/mol^{-1}. [59] When

temperature is increased, the weaker Cu-O bonds will be relatively easier to break than the

stronger Ta-O bonds. This type of layered structure is assumed to be responsible for the low

friction performance of this class of materials. [60]

2.1.2 $CuTa_2O_6$

The structure of $CuTa_2O_6$ is shown in Fig. 15 [61]. The space group for it is $P4_2/mnm$. The

structure of $CuTa_2O_6$ is related to rutile structure via triple stacking along the c-axis. [62] The

cations are surrounded by O^{2-} anions octahedra. These octahedras constitute edge-sharing chains.

[61] The consecutive Cu-O planes are separated by two Ta-O planes. The Cu and Ta cations

distribute randomly leading to disordered rutile structure. [62]
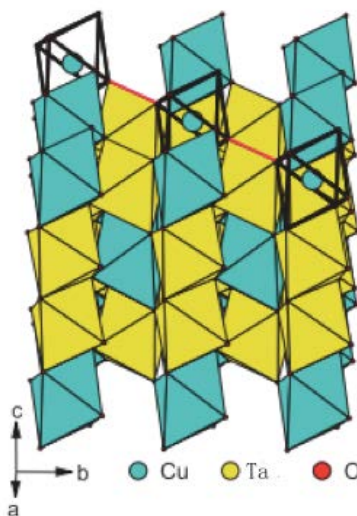
FIG 3 Crystal structure of $CuTa_2O_6$ with distorted oxygen octahedral around Cu and Ta drawn
with the respective colors. Red lines connecting open-face octahedral around Cu^{2+} indicate the
Cu-O-O-Cu bonds. [61]

The binding energy of O-O is 498.36 ± 0.17 KJ/mol^{-1} [59]. Compared with $CuTaO_3$, this

structure of $CuTa_2O_6$ shows that the friction coefficient might be higher than $CuTaO_3$ because

they do not have a layered structure.

2.2 X-ray Diffraction of Original Coatings

2.2.1 Powder
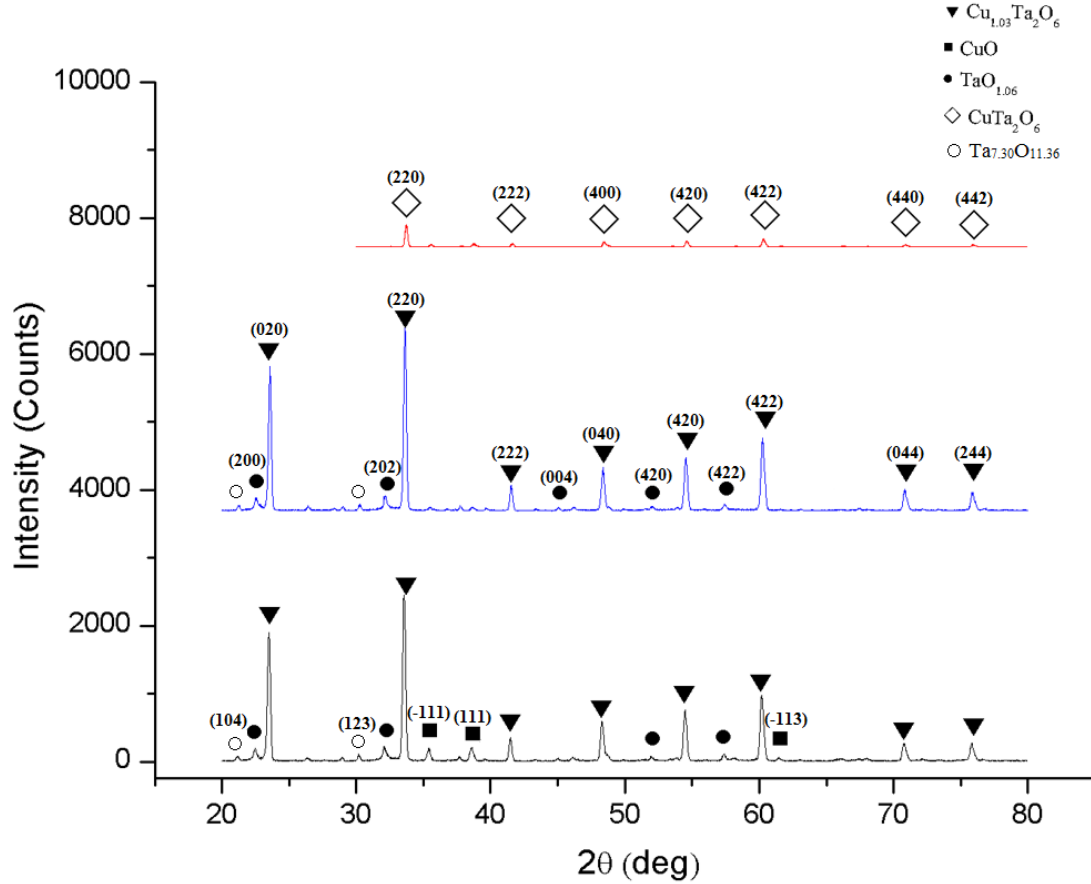
FIG 4 XRD patterns for Cu-Ta-O ternary oxides powder. Black line: G1; blue line: G2; red line: G3.

XRD of the powder samples was used to identify the phase composition of this material.

In Fig. 16, the black line, blue line, and red line represent samples G1, G2, and G3, respectively.

According to the XRD patterns, only $Cu_{1.03}Ta_2O_6$ and $CuTa_2O_6$ ternary phases were produced in

the selected deposition parameter range. Both $Cu_{1.03}Ta_2O_6$ and $CuTa_2O_6$ have orthorhombic crystal

structure with a=7.5228 Å and c=7.5199 Å. Their space group is Pmmm. The range of

$Cu_{1+x}Ta_2O_6$ with $0 \leq x \leq 0.30$ is a wide homogeneity range [48]; therefore, they can be considered as

the same phase. Because the purpose of this research is to study Cu-Ta-O ternary compound, we

will focus on the $Cu_{1.03}Ta_2O_6$ and $CuTa_2O_6$ phases for further evaluation. The most intense peak

corresponds to the (220) peak. This intense peak corresponds to $Cu_{1.03}Ta_2O_6$ phase (PDF Card

No. 01-070-0764). For the black and blue XRD patterns, sample G1 contains an additional phase

compared to G2, which means that the solid chemical reaction for Cu and Ta_2O_5 of G2 had a

more complete reaction than for G1. Compared to the black and red patterns, the peak intensities

for the patterns that correspond to sample G3 decreased dramatically, which means that the

crystallinity of sample G3 is reduced.

2.2.2 Sputtering

XRD of the samples produced by the sputtering method was used to identify the phase

composition of this material. In Fig. 17, the black, blue, and red lines represent samples S1, S2,

and S3, respectively. The analysis of these patterns revealed that Cu phases was the main phase

no matter what the selection of the sputtering power for Cu (set up the sputtering power of Ta as

a constant). The Cu phase has a cubic crystal structure with a=3.61 Å. The space group of Cu

phase is Fm3m. The relative intense peak is (111) peak. The most intense peak corresponds to

the Cu phase (PDF Card No. 01-071-4609). Further analysis of these peaks revealed that the

peak intensity of sample S1 decreased, which means that the crystallinity of sample S1 is low [63].

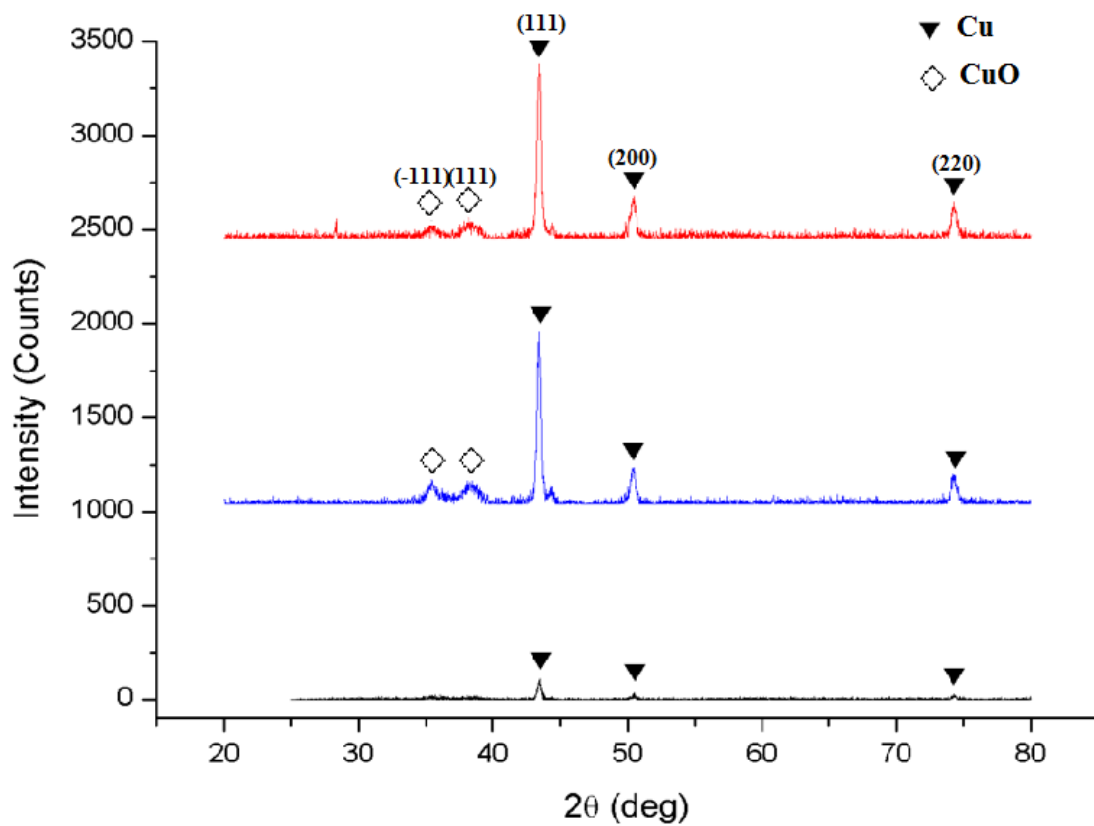FIG 5 XRD patterns for sputtering Cu-Ta-O ternary oxides. Black line: S1; blue line: S2; red line: S3.

2.3 Wear Testing

2.3.1 Powder

Table 1 Friction Coefficients of Burnished Powder Sample G2 at Different Temperature.

Sample	Room temperature	200 °C	430 °C
G2	0.5	0.35	0.45

The CoFs of the burnished powder sample G2 was studied from room temperature to

430 °C against a Si_3N_4 ball with an applied load of 2N. The CoFs for sample G2, shown in Table 6, revealed that the system has the lowest CoF at 200 °C. This phenomenon contradicts our hypothesis that the CoFs will decrease as the temperature increases.

We believe that this phenomenon is caused by the weak adhesion of the powder to the substrate. This weak adhesion causes the burnished coating to be easily removed by the moving Si_3N_4 ball. Therefore, the tribological results for powders are not conclusive.

2.3.2 Sputtering

Table 2 Friction Coefficients of Sputtering Sample S1 and S2 at Different Temperature.

Sample	Room temperature	200 °C	430 °C
S1	0.37	0.30	0.25
S2	0.38	0.35	0.23

The CoFs of the sputtering sample S1 and S2 was measured by using the same experimental procedure for burnished powder sample. The CoFs for sample S1 and S2, shown in Table 7, was discovered that the CoFs of the system was reduced as the temperature increased. These results are in aggreement with our hypothesis that the CoFs will decrease as the temperature is increased.

2.4 X-ray Diffraction of Coatings after Wear Testing

2.4.1 Powder
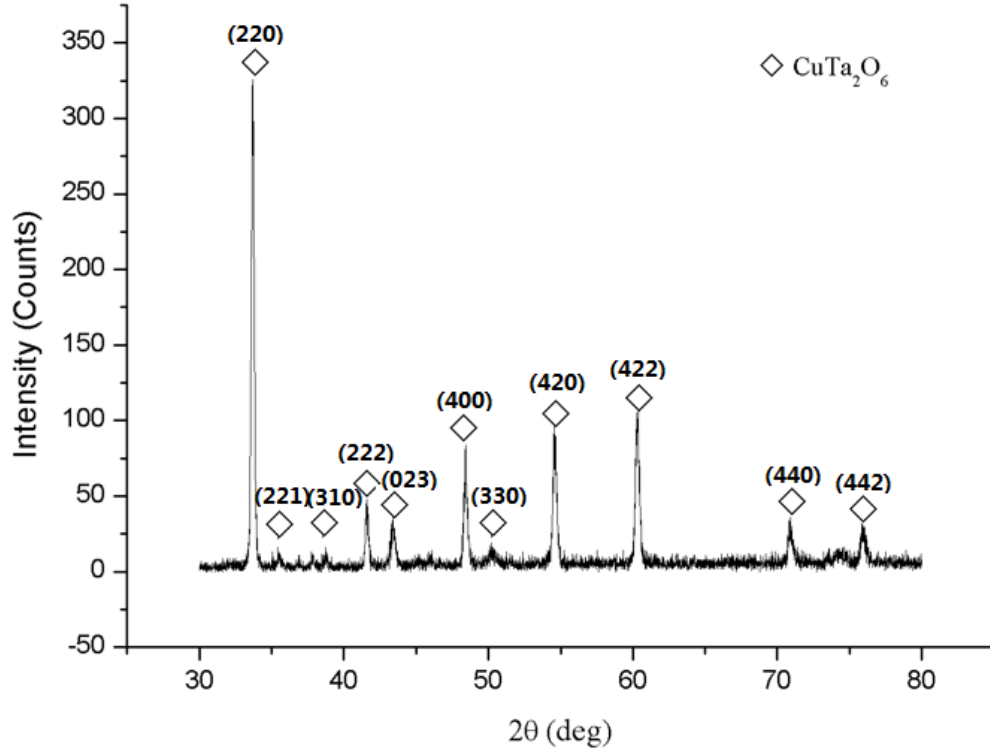
FIG 6 XRD patterns for Cu-Ta-O burnished powder after wear testing for sample G2.

XRD of the powder samples after wear testing was shown in Fig. 18, where the black line represents sample G2. According to these XRD patterns, only the $CuTa_2O_6$ ternary phase exists in these samples. $CuTa_2O_6$ has cubic crystal structure with a=7.517 Å. The relative intense peak is the (220) peak. The most intense peak corresponds to $CuTa_2O_6$ phase (PDF Card No. 00-024-0380). By comparing this XRD pattern with that of G2 before wear testing (blue line in Fig. 16), the orthorhombic crystal structure of $Cu_{1.03}Ta_2O_6$ changes to that of the cubic crystal structure of $CuTa_2O_6$.

2.4.2 Sputtering
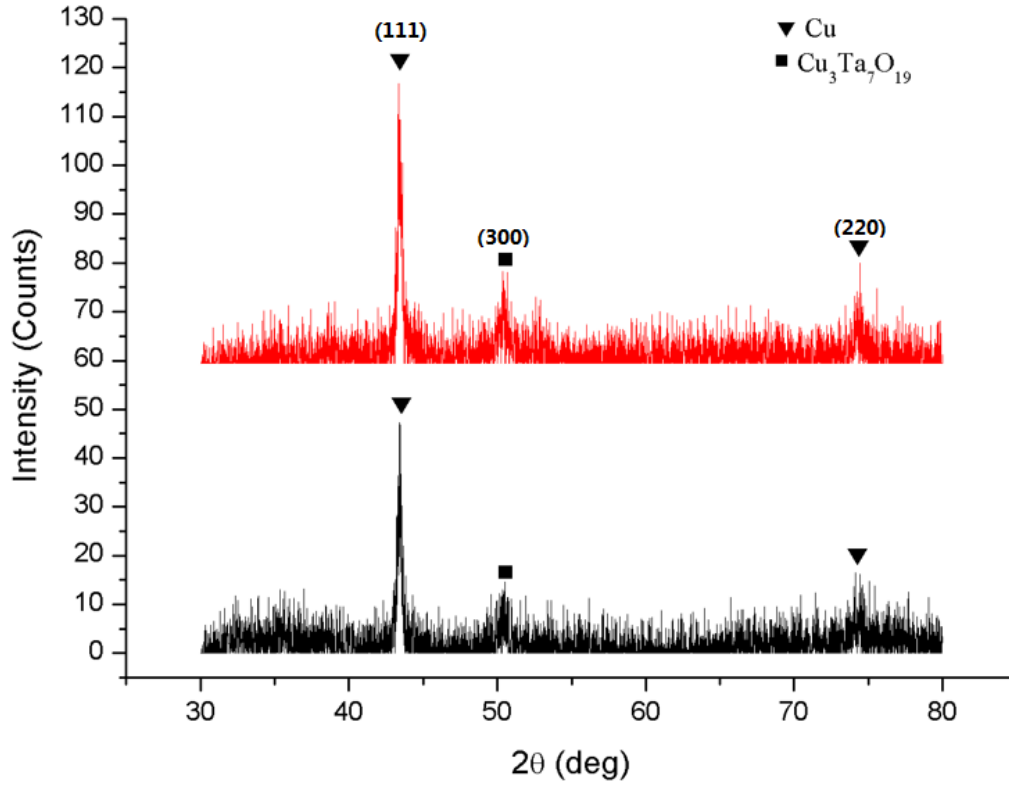
FIG 7 XRD patterns for sputtering Cu-Ta-O ternary oxides after wear testing for sample S1 and S2. Black line: S1; red line: S2.

XRD of the sputtering samples after wear testing was shown in Fig. 19, where the black line represents sample S1, and the red line represents S2. These XRD patterns reveal that the Cu phase and $Cu_3Ta_7O_{19}$ phases coexist. $Cu_3Ta_7O_{19}$ has a hexagonal crystal structure with a=7.517 Å, c=20.156 Å, and γ =120 °. The space group of $Cu_3Ta_7O_{19}$ is $P6_3/m$. The relative intense peak is (111) peak. The most intense peak corresponds to $CuTa_2O_6$ phase (PDF Card No. 01-081-0814). The Cu phase does not change. By comparing these XRD patterns with those of S1 and S2 before wear testing (black line and blue line in Fig. 17, separately), we can conclude that the hexagonal crystal structure of $Cu_3Ta_7O_{19}$ was formed during tribologial process.

41

2.5   Scanning Electron Microscopy

2.5.1   Sample S1

Figure 20 shows the surface morphology of three wear tracks that correspond to room temperature, 200 °C, and 430 °C tests. A slight overlap between the second and third wear track was observed, which might affect each others properties. This sample was not used for further evaluation. However, we can still notice that a new phase formed in the wear track based on the backscatter electron micrograph.

(a) (b)
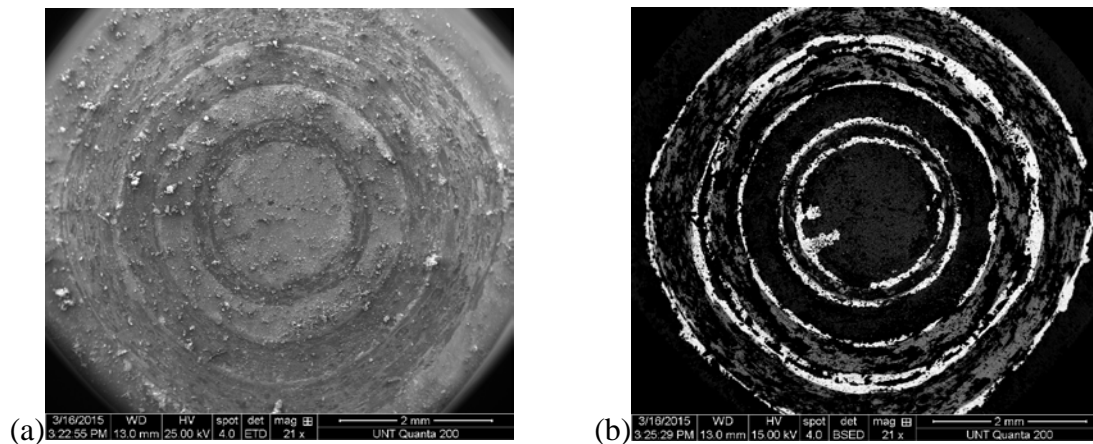
FIG 8 SEM micrograph of the wear track for the sputtering sample S1. (a) Secondary electron micrograph; (b) Backscatter electron micrograph.

2.5.2   Sample S2

Figure 21shows the surface morphology of three wear tracks for sample S2. These wear tracks correspond to tests conducted at room temperature, 200 °C, and 430 °C, repectively. In figure 21(a), two layers of the coating seem to exist. From room temperature to 430 °C, the area in the wear track become smoother. For the backscatter electron micrograph, from room temperature to 430 °C, there are some new phases that form after the tribological process. The

phases in the area near the wear track are different from those in the original coating.

(a)   (b)   (c)

(d)   (e)   (f)
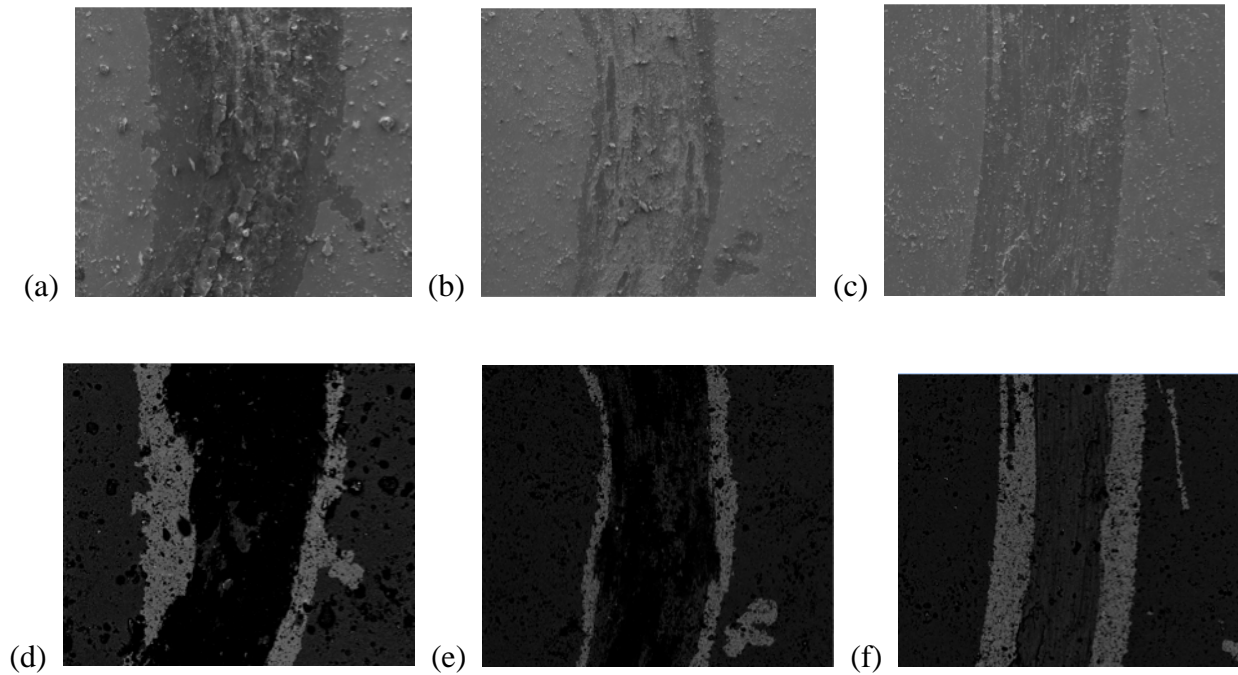
FIG 9 SEM micrograph of the wear track for the sputtering sample S2. (a), (b), and (c) are secondary electron micrograph for room temperature, 200 °C, and 430 °C, separately; (d), (e), and (f) are backscatter electron micrograph for room temperature, 200 °C, and 430 °C, separately.

The elemental composition in the different regions of the original coating and in the 430 °C wear track were evaluated by EDX. As shown in Fig. 22, the EDX result for the two different regions reveals that the content of Cu changes drastically compared to the other elements. The Cr and Ni content increases because the coating was worn out. Ta is present in the sputtering coating.
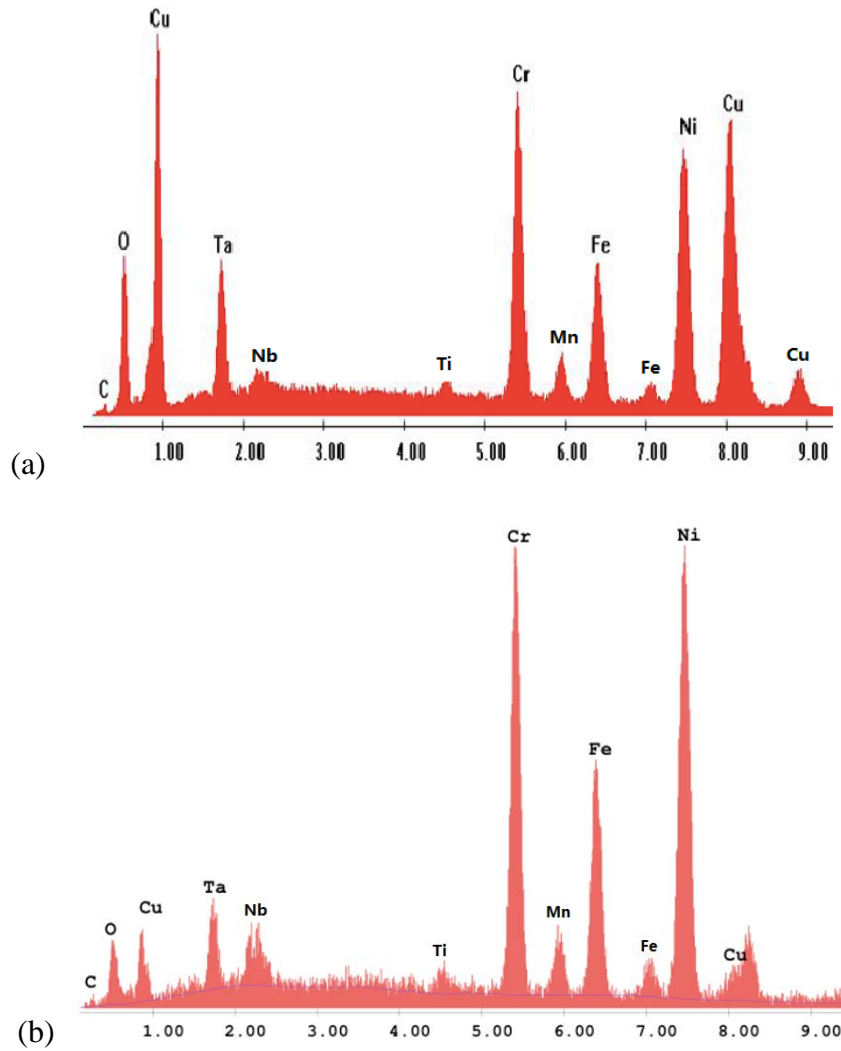
FIG 10 EDX spectrum of (a) original coating and (b) 430 °C wear track.

2.6 Auger Scanning Nanoprobe for Sample S2

2.6.1 Room Temperature

Fig. 23 shows an AES spectrum of a wear track surface for Cu-Ta-O ternary oxides (wear testing at room temperature). The intensity of the peaks that correspond to Cu, Ta, and O were measured around the wear track surface. The intensity of the Ta peak in areas 2 and 3 seems to be negligible. The surface of metals and ceramics is usually contaminated with carbon monoxide,

carbon dioxide, and oxide layers, and the contaminations will interfere with the electron signal from the tested material [64]. Therefore, a carbon contamination peak appeared in the Auger electron spectrum of the tested material. According to this Auger electron spectrum, the content of Cu is far more than the content of Ta. For the blue line, the content of Cu and Ta were reduced. The friction process resulted in a decrease in Cu and Ta content.

(a)

(b)

FIG 11 (a) Selected area for Auger scanning around wear track of room temperature; (b) Auger electron spectrum of selected area (red: area 1; blue: area 2; azure: area 3).

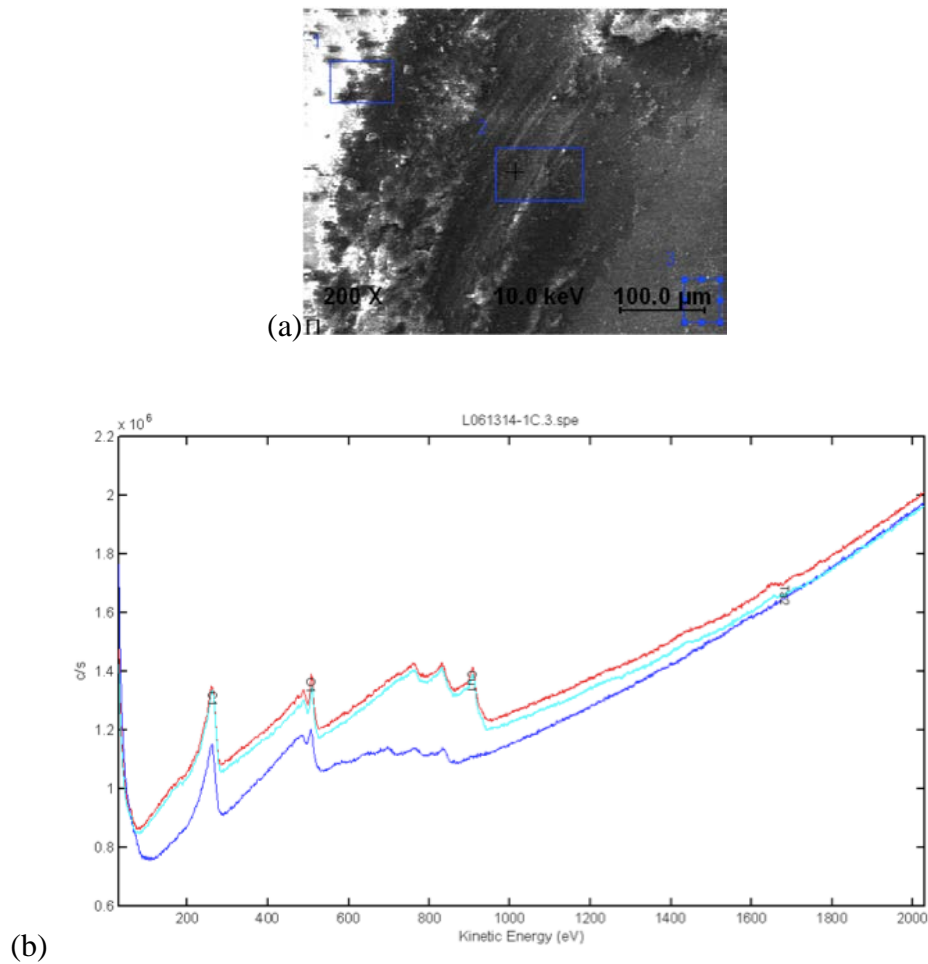The elemental mapping of the wear track and the original coating around the wear track was shown in Fig. 24. Due to the oxygen contamination [64], the content of oxygen is not accurate

and will not be considered. Fig. 24 (d) shows the selected area for the generation of the elemental

map. In Fig. 24, the content of Cu is very high. The Cu content in the original coating is more

than in the wear track because it was worn out by the wear process. Cu was found to be

uniformly distributed in the coating. Ta content is very low. The element distribution of Ta is

non-uniform.

FIG 12 Elemental mapping of selected area around wear track of room temperature. (a) Copper;
(b) Tantalum; (c) Oxygen; (d) Selected area.

2.6.2 200 °C

The AES spectrum of a wear track surface of the Cu-Ta-O ternary oxides (wear testing at

200 °C) was shown in Fig. 25. Cu, Ta, and O content was measured in the vicinity of the wear

track surface. The Ta peak in area 2 is negligible. A carbon contamination peak was present in

the Auger electron spectrum. According to this Auger electron spectrum, the content of Cu is also

far more than the content of Ta. For the blue line, the content of Cu and Ta were found to

decrease after wear testing.

(a)

(b)

FIG 13 (a) Selected area for Auger scanning around wear track of 200 °C; (b) Auger electron
spectrum of selected area (red: area 1; blue: area 2; azure: area 3).

Fig. 26 shows the elemental mapping of the wear track and the original coating around

the wear track. Oxygen is still not included in this data. In Fig. 26, the content of Cu is again

very high. The Cu in the original coating is more than in the wear track due to the wear process.

Cu was found to be uniformly distributed in the coating. Ta content is very low. The Ta is

distributed along the junction of the wear track and the original coating. No Ta was present in the surface of the wear track.
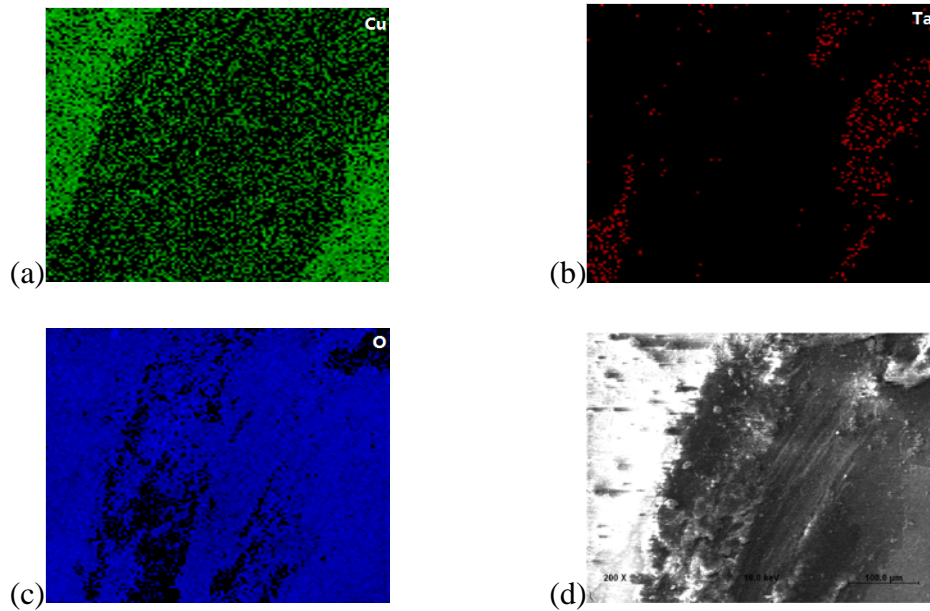

FIG 14 Elemental mapping of selected area around wear track of 200 °C. (a) Copper; (b) Tantalum; (c) Oxygen; (d) Selected area.

2.6.3   430 °C

After wear testing at 430 °C, the AES spectrum of the wear track surface of the Cu-Ta-O ternary oxides was shown in Fig. 27. The distribution of elemental Cu, Ta, and O were evaluated around the wear track surface. The Ta peak of area 2 is also negligible for this AES spectrum. A carbon contamination peak was present in the Auger electron spectrum of the tested material. According to this Auger electron spectrum, the content of Cu is still far more than the content of Ta. For the blue line, the content of Cu and Ta decreased dramatically as a result of the wear testing process.
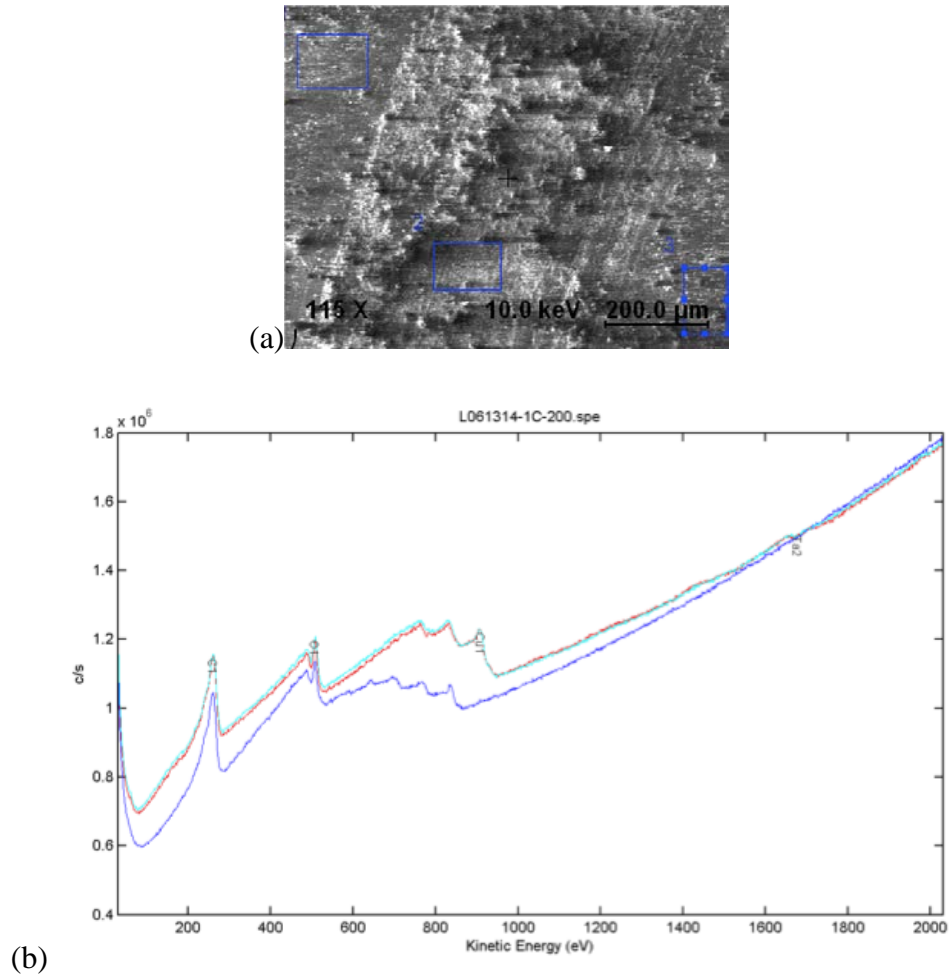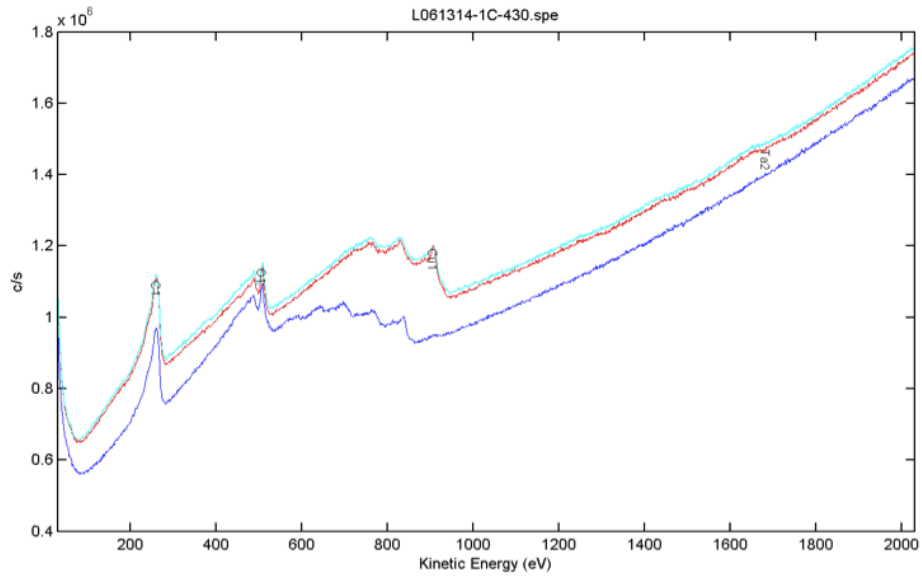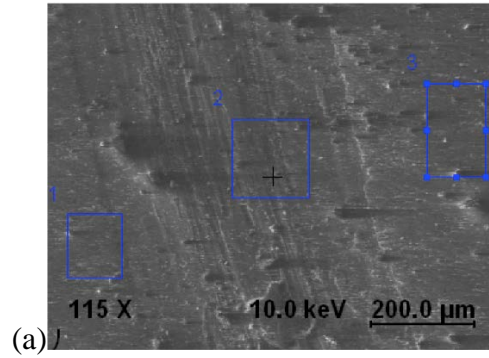
FIG 15 (a) Selected area for Auger scanning around wear track of 430 °C; (b) Auger electron spectrum of selected area (red: area 1; blue: area 2; azure: area 3).

In Fig. 28, the elemental mapping of the wear track and the original coating in the vicinity of the wear track was shown. Oxygen is not included in this data. The content of Cu is high, and the Cu in the original coating is more than in the wear track due to the wear process. Cu was uniformly distributed in the coating. For Ta, the content is very low. Along the junction of the wear track and the original coating, more Ta element is present. No Ta was detected in the surface of wear track.
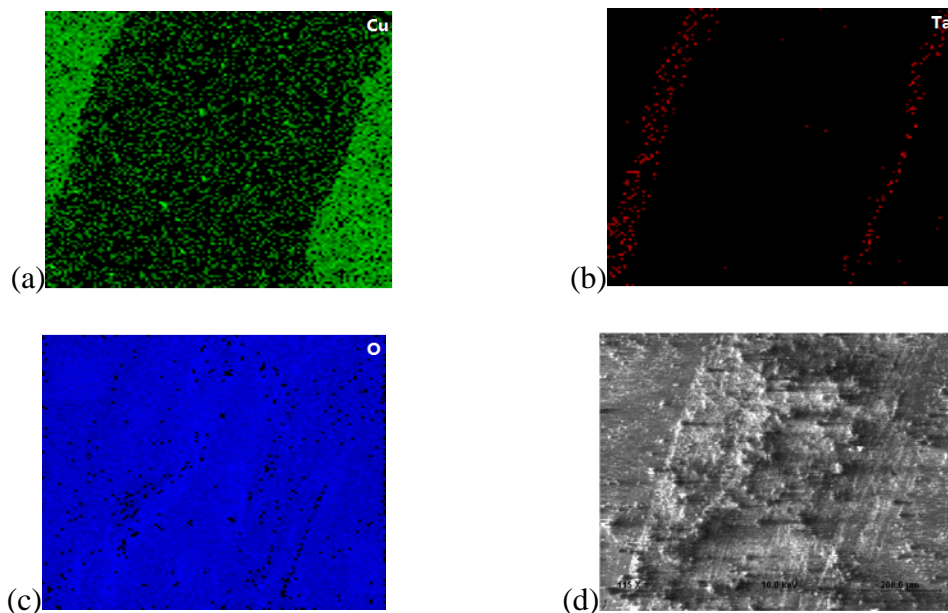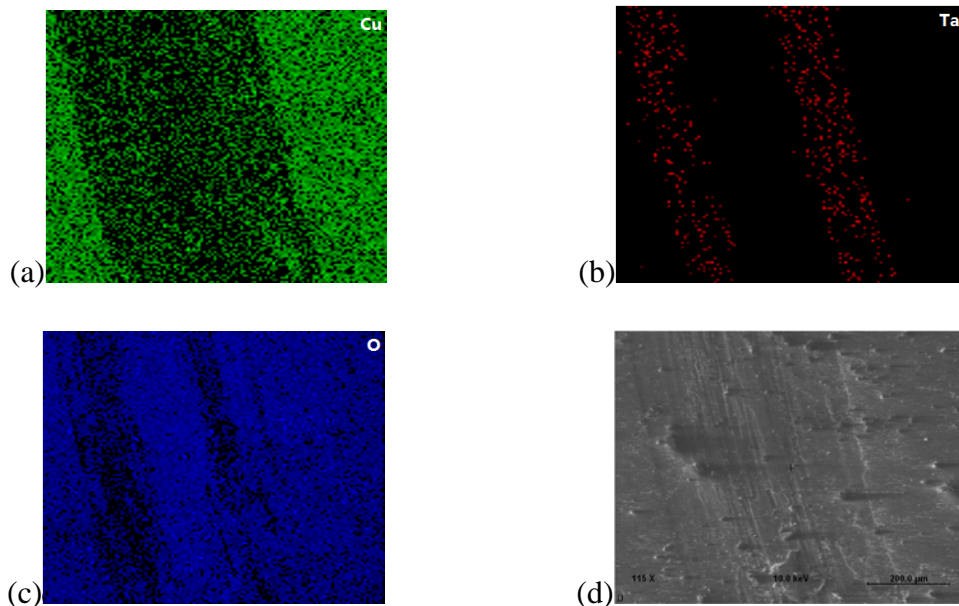
FIG 16 Elemental mapping of selected area around wear track of 430 °C. (a) Copper; (b) Tantalum; (c) Oxygen; (d) Selected area.

According to the elemental mapping for room temperature, 200 °C, and 430 °C testing, the content of Cu increased when temperature increased. From room temperature to 430 °C, the distribution of Ta became more uniformly distributed along the junction of the wear track and original coating.

2.7   X-ray Photoelectron Spectroscopy for Sample S2

In this experiment, the carbon contamination peak (C1s) was used to calibrate. The binding energy of C1s is 284.6 eV. The calibrate C1s peak was shown in Fig. 29 (a). The Cu2p and Ta4f XPS spectra are shown in Fig. 29 (b) and (c). Cu2p$_{3/2}$ shifted to high binding energy. CuO and Ta$_2$O$_5$ coexist in the original coating [65,66]. For room temperature tests, Ta$_2$O$_5$ was present in the surface of the wear track, but CuO disappeared. After wear testing at 430 °C, both

Ta_2O_5 and CuO disappeared.

FIG 17 X-ray photoelectron spectroscopy (XPS) spectra of sample S2. (a): Carbon; (b): Copper; (c) Tantalum. Black line represents the original coating. Blue line and red line represent wear track for room temperature testing and 430 °C testing, separately.

CHAPTER 3

SUMMARY, DISCUSSION, AND CONCLUSION AND RECOMMENDATION

3.1   Summary

The intrinsic properties and extrinsic performance of Cu-Ta-O ternary oxides were studied to explore their structural and tribological properties. These characteri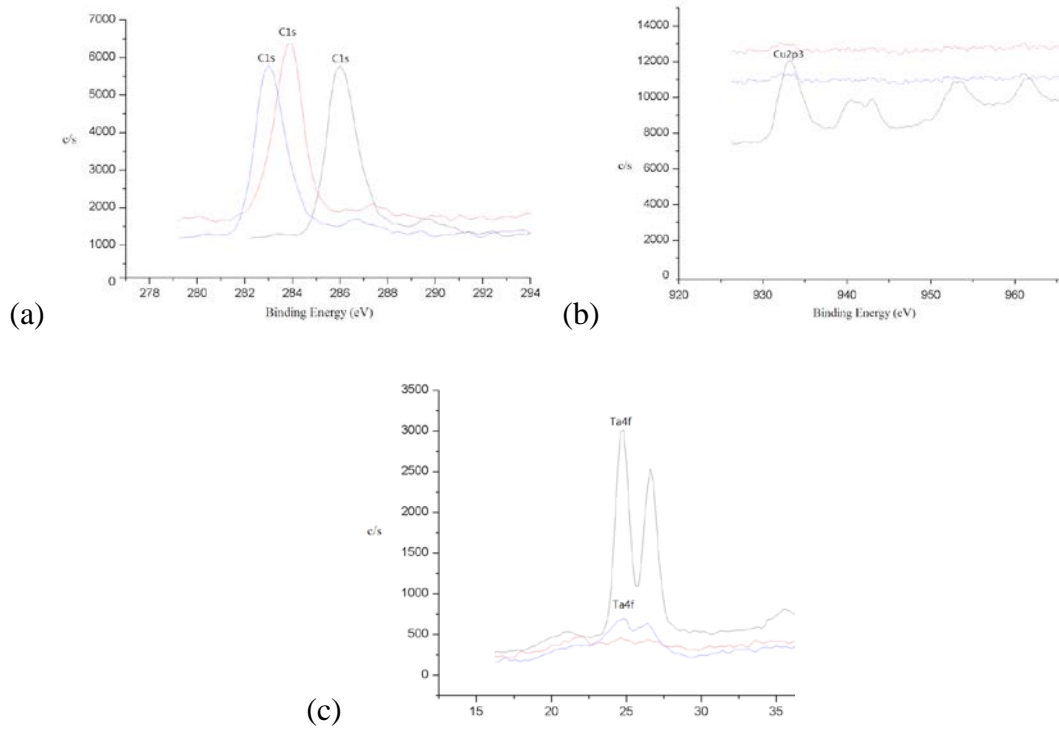stics have a great impact on the operation of the tribology system under varying circumstances such as aerospace industry. Creating nanocomposite adaptive coatings depends on the design of Cu-Ta-O lubricious ternary oxides combining transitional metal and soft metal. During this research process, the powder oxides $CuTa_2O_6$ and the sputtering nanocomposite coatings of Cu-Ta-O were respectively tested by tribometer in room temperature, 150 °C, and 430 °C to identify their tribological properties in severe conditions.

X-ray diffraction, friction testing, scanning electron microscope, Auger scanning nanoprobe, and XPS were applied to search the mechanism for the tribological behavior of Cu-Ta-O ternary oxides. Due to the superior tribological performance of $AgTaO_3$, copper was selected to instead silver because they belong to the same group of the periodic table of the elements. The powder samples are $CuTa_2O_6$ which has tri-rutile structure. For the sputtering samples, they have hexagonal structure of $Cu_3Ta_7O_{19}$ after tribological test. The two oxides have different crystal structure, which in turn have different tribological response.

The crystal structure of $CuTa_2O_6$ is that Cu and Ta cations are octahedrally surrounded by O^{2-}. These octahedras share their edge to form chains. [7] Two Ta-O planes separate consecutive Cu-O planes. The randomly distribution of Cu and Ta results in a disordered rutile structure. [8]

Compared with $CuTaO_3$ (perovskite), this nonlayered structure of $CuTa_2O_6$ shows that the friction coefficient might be higher than $CuTaO_3$.

For tribological testing, both S1 and S2 sputtered samples reveal a decrease in friction coefficient from room temperature to 430 °C. However, the CoFs of powder samples decreased firstly (at 200 °C) and then increased. The reason may be attributed to the weak adhesion of the powder to the substrate. The CoFs for powder burnished sample changed from 0.5 at room temperature to 0.45 at 200 °C and then 0.45 at 430 °C. For the sputtering samples, the CoFs was found to vary from 0.38 at room temperature to 0.23 at 430 °C. XRD, SEM, AES, and XPS were used to explore the tribological mechanism of these coatings after testing. XRD results for the $CuTa_2O_6$ powder sample showed that phase transformation of $CuTa_2O_6$ occurred. For sputtering samples, XRD results revealed the formation of the $Cu_3Ta_7O_{19}$ phase.

SEM analysis revealed that phase transformation occurred in the sputtered samples. AES data revealed that the content of Cu increased when temperature increased. From room temperature to 430 °C, the distribution of Ta became more uniform at the edge of the wear track. Also, CuO and Ta_2O_5 were found to coexist in the original coating of the sputtered samples.

3.2   Discussion

Due to the superior lubricious performance of $AgTaO_3$, this study was focused on $CuTaO_3$ lubricious coatings because their layered crystal structure (perovskite) is the same as $AgTaO_3$ and could reduce the friction. However, both solid chemical synthesis and sputtering method failed to create $CuTaO_3$, because $CuTaO_3$ phases can only be obtained at high pressure [67].

Based on the experimental studies, compared with $AgTaO_3$, the friction coefficients decreased with temperature was increased. The friction coefficients of Cu-Ta-O ternary oxides are higher than $AgTaO_3$ because copper is less mobile that silver. However, silver can migrate and contaminate the surrounding components. Copper might provide an alternative when this problem arises in a given application.

Based on the theoretical studies (Molecular dynamics simulation), the result shows the friction properties that $f_{(AgTaO3)} < f_{(CuTaO3)} < f_{(CuTa2O6)}$, which has a good agreement with experimental methods. The wear performance of Cu-Ta-O ternary oxides is better than $AgTaO_3$, which means that Cu-Ta-O ternary oxides are harder than $AgTaO_3$, because the copper clusters (soft phase) are less than silver clusters at the sliding surfaces. Therefore, the Cu-Ta-O ternary oxides cannot be easily worn out during tribological process.

Finally, the friction performance of $CuTaO_3$, $CuTa_2O_6$, and $AgTaO_3$ is

$AgTaO_3 > CuTaO_3 > CuTa_2O_6$, and the wear performance of these three materials is $AgTaO_3 < CuTaO_3 < CuTa_2O_6$. These result shows that $AgTaO_3$ has the lowest friction coefficient, and $CuTa_2O_6$ has the highest hardness. Because the measurements of tribological performance for materials are not only considered the friction performance but also wear performance, $CuTaO_3$ is the promising material in this study.

3.3   Conclusion and Recommendation

In this research, the relationship between crystal structure and tribological performance under high temperature environment was investigated for Cu-Ta-O ternary oxides. Compared

with AgTaO$_3$, Cu-Ta-O ternary oxides were also available materials to decrease friction with temperature increased from 25°C to 1000 °C range, which showed the same trend as AgTaO$_3$.

These elements, when deposited by sputtering or solid chemical synthesis, produce ternary oxides participating the tribological process during tribotesting. These ternary oxides have weak interplanar bonds due to the layered crystal structure. These weak interplanar bonds result in materials prone to shearing and exhibit low friction coefficients. The copper clusters were formed at the sliding surface during the tribological process to reduce the friction coeffiecients. The wear performance of Cu-Ta-O ternary oxides is better than Ag-Ta-O ternary oxides.

For further research, several recommendations can be chosen. Firstly, the adhesion of powders on the substrate should be addressed. Secondly, due to the friction and wear performances of CuTaO$_3$ are ranged between AgTaO$_3$ and CuTa$_2$O$_6$, CuTaO$_3$ is the best candidate for high temperature solid lubricant compared to AgTaO$_3$ and CuTa$_2$O$_6$. Therefore, the stoichiometric chemical composition of Cu-Ta-O ternary oxides needs to be optimized to obtain CuTaO$_3$. This research will help us to gain an insight into further studies of promising material for high temperature tribological applications.

APPENDIX

MOLECULAR DYNAMICS SIMULATION

For the molecular dynamics (MD) simulation, special potential parameters for $CuTaO_3$ and $CuTa_2O_6$ were generated to study their tribological properties. The modified embedded atom method (MEAM) was used to develop potential parameters for Cu-Ta-O ternary oxide[1]. $CuTaO_3$ (Z=1) and $CuTa_2O_6$ (Z=4) were defined as cubic cell. A plane-wave cut-off of 520eV was used in all cases. For $CuTaO_3$ and $CuTa_2O_6$, a 14×14×14 k-point grid and a 6×6×6 k-point grid were applied, respectively. The LAMMPS[2] was used for fitting potential parameters of $CuTaO_3$ and $CuTa_2O_6$.

Two sliding models were created to investigate the tribological properties of Cu-Ta-O ternary oxides. Model 1 is a plate-on-plate model to analyze the evolution of the film reconstruction, and model 2 is a ball-on-plate model to study the transfer and wear of these materials. The two models were simulated at room temperature and 750 °C.

Figure A.1(a) illustrates the friction coefficients for $AgTaO_3$, $CuTaO_3$, and $CuTa_2O_6$ from MD and experiment under 750 °C. Based on these two figures, the friction coefficients of MD show the result that f ($AgTaO_3$) < f ($CuTaO_3$) < f ($CuTa_2O_6$), and exhibit the same trend as the experimental results. From figure A.1(b), the friction coefficients of these three materials (from MD and experiment) decreased with temperature increased. In figure A.1(c), the numbers of Ag and Cu clusters for $AgTaO_3$ and $CuTaO_3$ were compared. These two curves increased from 0 to 2 ns, then they reached equilibrium. The number of Cu clusters is half less than Ag at equilibrium. Due to the friction correlated to the number of Ag/Cu clusters (soft metal phase), the friction coefficients of $CuTaO_3$ is higher than $AgTaO_3$. The wear performance of the solid lubricant is another factor which can influence the tribological properties of the materials. The

wear depth of these three materials was measured in figure 30(d) at 750 °C. From the figure

A.1(d), the trend of the wear depth for $AgTaO_3$, $CuTaO_3$, and $CuTa_2O_6$ was d ($AgTaO_3$) > d

($CuTaO_3$) > d ($CuTa_2O_6$). This result indicates that $AgTaO_3$ can be easily worn out than $CuTaO_3$

and $CuTa_2O_6$, which means that Cu-Ta-O ternary oxides are harder than $AgTaO_3$.

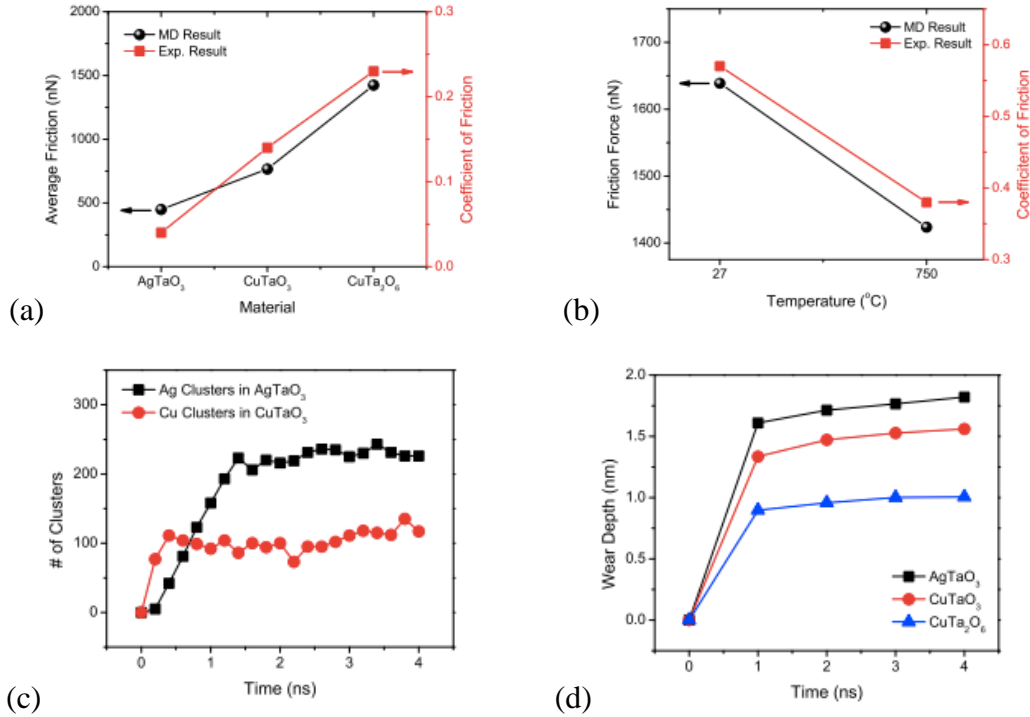FIG 18 MD- and experiment-predicted friction as functions of (a) material and (b) temperature; (c) Number of clusters as a function time; (d) MD-predicted wear depth.

1. M. Baskes. Modified embedded-atom potentials for cubic materials and impurities. Phys. Rev. B, 46:2727–2742, Aug 1992.

2. Steve Plimpton. Fast parallel algorithms for short-range molecular dynamics. Journal of Computational Physics, 117(1):1 – 19, 1995.

REFERENCES

1. Lubricant. (n.d.). Retrieved March 1, 2015, from https://en.wikipedia.org/wiki/Lubricant.

2. Clauss, F. (1972). Solid lubricants and self-lubricating solids. New York: Academic Press.

3. Bhushan, B. (2001). Modern tribology handbook. Boca Raton, FL: CRC Press.

4. Miyoshi, K. (Ed.). (2001). Solid lubrication fundamentals and applications. CRC Press.

5. Donnet, C., & Erdemir, A. (2004). Historical developments and new trends in tribological and solid lubricant coatings. Surface and Coatings Technology,180, 76-84.

6. Voevodin, A. A., & Zabinski, J. S. (2005). Nanocomposite and nanostructured tribological materials for space applications. Composites Science and Technology, 65(5), 741-748.

7. Allam, I. M. (1991). Solid lubricants for applications at elevated temperatures. Journal of Materials Science, 26(15), 3977-3984.

8. Baker, C. C., Chromik, R. R., Wahl, K. J., Hu, J. J., & Voevodin, A. A. (2007). Preparation of chameleon coatings for space and ambient environments. Thin Solid Films, 515(17), 6737-6743.

9. Miyoshi, K. (2007). Solid lubricants and coatings for extreme environments: state-of-the-art survey.

10. Bhushan, B. (2013). Introduction to tribology (Second ed.). New York: John Wiley & Sons.

11. Mang, T., Bobzin, K., & Bartels, T. (2011). Industrial tribology: tribosystems, friction, wear and surface engineering, lubrication. John Wiley & Sons.

12. Bhushan, B. (Ed.). (2010). Handbook of micro/nano tribology. CRC press.

13. Schmalzried, H. (2008). Chemical kinetics of solids. John Wiley & Sons.

14. Muratore, C., & Voevodin, A. A. (2009). Chameleon coatings: adaptive surfaces to reduce friction and wear in extreme environments. Annual Review of Materials Research, 39, 297-324.

15. Holmberg, K., & Mathews, A. (1994). Coatings tribology: a concept, critical aspects and future directions. Thin Solid Films, 253(1), 173-178.

16. Aouadi, S. M., Gao, H., Martini, A., Scharf, T. W., & Muratore, C. (2014). Lubricious oxide coatings for extreme temperature applications: A review Surface and Coatings Technology, 257, 266-277.

17. Miyoshi, K. (n.d.). Solid Lubricants and Coatings for Extreme Environments: State-of-the-Art Survey. NASA Technical Reports Server (NTRS). Retrieved March 1, 2015, from http://ntrs.nasa.gov/archive/nasa/casi.ntrs.nasa.gov/20070010580.pdf.

18. Teer, D. (n.d.). New Solid Lubricant Coatings. Wear, 1068-1074.

19. Erdemir, A. (2005). Review of engineered tribological interfaces for improved boundary lubrication. Tribology International, 38(3), 249-256.

20. Erdemir, A. (2000). A crystal-chemical approach to lubrication by solid oxides. Tribology Letters, 8(2-3), 97-102.

21. Zabinski, J. S., Corneille, J., Prasad, S. V., Mc Devitt, N. T., & Bultman, J. B. (1997). Lubricious zinc oxide films: synthesis, characterization and tribological behaviour. Journal of materials science, 32(20), 5313-5319.

22. Erdemir, A. (2005). Review of engineered tribological interfaces for improved boundary lubrication. Tribology International, 38(3), 249-256.

23. Erdemir, A. (2000). A crystal-chemical approach to lubrication by solid oxides. Tribology Letters, 8(2-3), 97-102.

24. Hauert, R., & Patscheider, J. (2000). From alloying to nanocomposites—Improved performance of hard coatings. Advanced Engineering Materials,2(5), 247-259.

25. Pande, C. S., & Cooper, K. P. (2009). Nanomechanics of Hall–Petch relationship in nanocrystalline materials. Progress in Materials Science, 54(6), 689-706.

26. Zhang, S., Sun, D., Fu, Y., & Du, H. (2003). Recent advances of superhard nanocomposite coatings: a review. Surface and Coatings Technology, 167(2), 113-119.

27. Voevodin, A. A., Muratore, C., & Aouadi, S. M. (2014). Hard coatings with high temperature adaptive lubrication and contact thermal management: review. Surface and Coatings Technology, 257, 247-265.

28. Muratore, C., & Voevodin, A. A. (2006). Molybdenum disulfide as a lubricant and catalyst in adaptive nanocomposite coatings. Surface and Coatings Technology, 201(7), 4125-4130.

29. Stone, D. S., Harbin, S., Mohseni, H., Mogonye, J. E., Scharf, T. W., Muratore, C., ... & Aouadi, S. M. (2013). Lubricious silver tantalate films for extreme temperature applications. Surface and Coatings Technology, 217, 140-146.

30. Stone, D. S., Gao, H., Chantharangsi, C., Paksunchai, C., Bischof, M., Jaeger, D., ... & Aouadi, S. M. (2014). Load-dependent high temperature tribological properties of silver tantalate coatings. Surface and Coatings Technology, 244, 37-44.

31. Cushen, M., Kerry, J., Morris, M., Cruz-Romero, M., & Cummins, E. (2013). Migration and exposure assessment of silver from a PVC nanocomposite. Food chemistry, 139(1), 389-397.

32. Manninen, N. K., Ribeiro, F., Escudeiro, A., Polcar, T., Carvalho, S., & Cavaleiro, A. (2013). Influence of Ag content on mechanical and tribological behavior of DLC coatings. Surface and Coatings Technology, 232, 440-446.

33. Huheey, J. E., Keiter, E. A., Keiter, R. L., & Medhi, O. K. (2006). Inorganic chemistry: principles of structure and reactivity. Pearson Education India.

34. De Graef, M., & McHenry, M. E. (2007). Structure of materials: an introduction to crystallography, diffraction and symmetry. Cambridge University Press.

35. Madelung, O. (2000). Ternary compounds, organic semiconductors: Supplement to vol. III/17h, i (print version), revised and updated edition of vol. III/17h, i (CD-ROM) (New series. ed.). Berlin: Springer.

36. Data from Bowden, F.P. and Tabor, D. (1954), Friction and lubrication of solids, I, Clarendon Press, Oxford.

37. Gulbiński, W., Suszko, T., Sienicki, W., & Warcholiński, B. (2003). Tribological properties of silver-and copper-doped transition metal oxide coatings. Wear, 254(1), 129-135.

38. Kania, A. (2001). Dielectric properties of Ag1-xAxNbO3 (A: K, Na and Li) and AgNb1-xTaxO3 solid solutions in the vicinity of diffuse phase transitions. Journal of Physics D: Applied Physics, 34(10), 1447.

39. Lichtenberg, F., Herrnberger, A., & Wiedenmann, K. (2008). Synthesis, structural, magnetic and transport properties of layered perovskite-related titanates, niobates and tantalates of the type AnBnO3n+2, A′ Ak− 1BkO3k+ 1 and AmBm− 1O3m. Progress in Solid State

Chemistry, 36(4), 253-387.

40. Mattox, D. M. (2010). Handbook of physical vapor deposition (PVD) processing. William Andrew.

41. Schuegraf, K. K. (1988). Handbook of thin-film deposition processes and techniques: principles, methods, equipment, and applications. Noyes Data Corporation/Noyes Publications.

42. Ohring, M. (2001). Materials science of thin films. Academic press.

43. Seshan, K. (2001). Handbook of thin film deposition. William Andrew.

44. Kelly, P. J., & Arnell, R. D. (2000). Magnetron sputtering: a review of recent developments and applications. Vacuum, 56(3), 159-172.

45. Materials and Methods. (n.d.). Retrieved March 1, 2015, from http://magnetron.drujba.org/materials-and-methods.

46. Magnetron Sputter Deposition. (n.d.). Retrieved March 1, 2015, from http://www.oxford-instruments.com/products/etching-deposition-and-growth/plasma-etch-deposition/physical-vapour-deposition-(pvd).

47. West, A. R. (2007). Solid state chemistry and its applications. John Wiley & Sons.

48. ILUNGA, P. (1983). Phase analysis studies in the system Cu2O-CuO—Ta2O5. ACTA CHEMICA SCANDINAVICA SERIES A-PHYSICAL AND INORGANIC CHEMISTRY, 37(2), 117-123.

49. Kalantar-zadeh, K., & Fry, B. (2007). Nanotechnology-enabled sensors. Springer Science & Business Media.

50. Birkholz, M. (2006). Thin film analysis by X-ray scattering. John Wiley & Sons.

51. Microscopy and microanalysis - FEI Quanta 200 ESEM FEG. (n.d.). Retrieved March 2, 2015, from http://www.fy.chalmers.se/microscopy/instrumentation/SEM/ESEM.xml

52. Khursheed, A. (2011). Scanning electron microscope optics and spectrometers. World

Scientific.

53. Johansson, I., & Somasundaran, P. (Eds.). (2007). Handbook for cleaning/decontamination of surfaces. Elsevier.

54. Brune, D., Hellborg, R., Whitlow, H. J., & Hunderi, O. (Eds.). (2008). Surface characterization. John Wiley & Sons.

55. Hofmann, S. (2012). Auger-and X-ray photoelectron spectroscopy in materials science: a user-oriented guide (Vol. 49). Springer Science & Business Media.

56. Van der Heide, P. (2011). X-ray photoelectron spectroscopy: an introduction to principles and practices. John Wiley & Sons.

57. Madelung, O., Rössler, U., & Schulz, M. (2000). Ternary compounds, organic semiconductors. Landolt-Bönste in, Condensed Matter, Subvolume III E, 41, 471-477.

58. Retrieved March 11, 2015, from http://som.web.cmu.edu/StructuresAppendix2.pdf

59. Retrieved March 11, 2015, from http://staff.ustc.edu.cn/~luo971/2010-91-CRC-BDEs-Tables.pdf

60. Stone, D., Liu, J., Singh, D. P., Muratore, C., Voevodin, A. A., Mishra, S., ... & Aouadi, S. M. (2010). Layered atomic structures of double oxides for low shear strength at high temperatures. Scripta Materialia, 62(10), 735-738.

61. Retrieved March 12, 2015, from http://www2.fkf.mpg.de/cs/docs/ar/jb2003.pdf

62. Kinast, E. J., Zawislak, L. I., Da Cunha, J. B. M., Antonietti, V., De Vasconcellos, M. A. Z., & Dos Santos, C. A. (2002). Coexistence of rutile and trirutile phases in a natural tapiolite sample. Journal of Solid State Chemistry,163(1), 218-223.

63. Waseda, Y., Matsubara, E., & Shinoda, K. (2011). X-ray diffraction crystallography: introduction, examples and solved problems. Springer Science & Business Media.

64. Miyoshi, K., & Chung, Y. W. (Eds.). (1993). Surface diagnostics in tribology: fundamental principles and applications (Vol. 1). World scientific.

65. Hofmann, S. (2012). Auger-and X-ray photoelectron spectroscopy in materials science: a

user-oriented guide (Vol. 49). Springer Science & Business Media.

66. Atuchin, V. V., Grivel, J. C., & Zhang, Z. (2009). Core level photoemission spectroscopy and chemical bonding in Sr2Ta2O7. Chemical Physics,360(1), 74-78.

67. Sleight, A. W., & Prewitt, C. T. (1970). Preparation of CuNbO3 and CuTaO3 at high pressure. Materials Research Bulletin, 5(3), 207-211.